JGR Space Physics

RESEARCH ARTICLE
10.1029/2021JA029871

Energetic Electron Precipitation Driven by the Combined Effect of ULF, EMIC, and Whistler Waves

M. Fraz Bashir[1], Anton Artemyev[1], Xiao-Jia Zhang[1], and Vassilis Angelopoulos[1]

[1]Earth, Planetary, and Space Sciences, University of California, Los Angeles, Los Angeles, CA, USA

Key Points:

- Ultra-low-frequency (ULF) waves may drive electron precipitation via successive electron interactions with ULF-driven electromagnetic ion cyclotron (EMIC) and whistler waves
- Hot plasma effects on minimum resonant electron energy are negligible for high-frequency hydrogen-band EMIC waves
- Nonlinear electron interactions with whistler waves affect the net electron precipitation rates

Supporting Information:

Supporting Information may be found in the online version of this article.

Correspondence to:

M. F. Bashir,
frazbashir@epss.ucla.edu

Citation:

Bashir, M. F., Artemyev, A., Zhang, X.-J., & Angelopoulos, V. (2022). Energetic electron precipitation driven by the combined effect of ULF, EMIC, and whistler waves. *Journal of Geophysical Research: Space Physics*, *127*, e2021JA029871. https://doi.org/10.1029/2021JA029871

Received 11 AUG 2021
Accepted 16 DEC 2021

Abstract Energetic electron losses in the Earth's inner magnetosphere are dominated by outward radial diffusion and scattering into the atmosphere by various electromagnetic waves. The two most important wave modes responsible for electron scattering are electromagnetic ion cyclotron (EMIC) waves and whistler-mode waves (whistler waves) that, acting together, can provide rapid electron losses over a wide energy range from few keV to few MeV. Wave-particle resonant interaction resulting in electron scattering is well described by quasi-linear diffusion theory using the cold plasma dispersion, whereas the effects of nonlinear resonances and hot plasma dispersion are less well understood. This study aims to examine these effects and estimate their significance for a particular event during which both wave modes are quasi-periodically modulated by ultra-low-frequency (ULF) compressional waves. Such modulation of EMIC and whistler wave amplitudes provides a unique opportunity to compare nonlinear resonant scattering (important for the most intense waves) with quasi-linear diffusion (dominant for low-intensity waves). The same modulation of plasma properties allows better characterization of hot plasma effects on the EMIC wave dispersion. Although hot plasma effects significantly increase the minimum resonant energy, E_{min}, for the most intense EMIC waves, such effects become negligible for the higher frequency part of the hydrogen-band EMIC wave spectrum. Nonlinear phase trapping of 300–500 keV electrons through resonances with whistler waves may accelerate and make them resonant with EMIC waves that, in turn, quickly scatter those electrons into the loss-cone. Our results highlight the importance of nonlinear effects for simulations of energetic electron fluxes in the inner magnetosphere.

1. Introduction

Energetic electron fluxes at Earth's inner magnetosphere are controlled by a fine balance between various losses and acceleration mechanisms (Lyons & Williams, 1984; Schulz & Lanzerotti, 1974). Wave-particle resonant interaction is a very important component of this balance (see discussion in Thorne, 2010; Ukhorskiy et al., 2011). There are many plasma waves responsible for energetic electron scattering into the loss-cone or acceleration (W. Li & Hudson, 2019; Millan & Baker, 2012; Millan & Thorne, 2007), but the most intense and effective are electromagnetic whistler-mode waves and electromagnetic ion-cyclotron (EMIC) waves. Whistler-mode waves (whistler waves) scatter plasma sheet 1–100 keV electrons (Kasahara et al., 2018; Nishimura et al., 2011), or accelerate them to relativistic energies (Allison & Shprits, 2020; Horne et al., 2005; W. Li et al., 2014; Mourenas, Artemyev, Agapitov, Krasnoselskikh, et al., 2014; Thorne et al., 2010), depending on geomagnetic conditions and background plasma parameters (Agapitov et al., 2018; Meredith et al., 2001, 2003; Wang & Shprits, 2019). EMIC waves are responsible for extremely fast losses (due to scattering into the loss-cone) of relativistic electrons (Bashir & Ilie, 2018; Drozdov et al., 2017; Ma et al., 2015; Ni et al., 2015; Shprits et al., 2016; Ukhorskiy et al., 2010; Yahnin et al., 2016; Zhang et al., 2021; Zhang, Li, Ma, et al., 2016). These two modes acting together can quickly reduce relativistic electron fluxes within a wide pitch-angle range (Mourenas, Artemyev, Ma, et al., 2016; Shprits et al., 2017; Zhang et al., 2017).

Both whistler and EMIC wave statistical observations have been well-documented (Agapitov et al., 2013, 2015; Kersten et al., 2014; Meredith et al., 2012; Wang et al., 2019; Zhang, Li, Thorne, et al., 2016) and incorporated into global radiation belt models (e.g., Drozdov et al., 2015; Ma et al., 2018). EMIC waves can scatter relativistic electrons within a small pitch-angle range around the loss-cone (e.g., Blum et al., 2015; Capannolo, Li, Ma, Chen, et al., 2019; Capannolo, Li, Ma, Shen, et al., 2019; Z. Li et al., 2014), and whistler waves are effective in relativistic electron scattering over the wider pitch-angle range (e.g., Glauert & Horne, 2005; Horne et al., 2013). The combined EMIC-whistler mode effect consists of relativistic electron scattering by whistler waves from high to intermediate or low pitch-angles, where these electrons may, in turn, resonate with EMIC waves and be quickly scattered further into the loss-cone (Mourenas, Artemyev, Ma, et al., 2016). Such combined scattering

seems to be an effective mechanism of relativistic electron losses, but it has been investigated mostly within the classical paradigm of quasi-linear electron diffusion by waves described by the cold plasma dispersion. Two main effects that may alter this combined scattering are nonlinear resonances and the hot plasma contribution to wave dispersion.

Resonant electron scattering by whistler or EMIC waves is traditionally described by the quasi-linear theory (Andronov & Trakhtengerts, 1964; Kennel & Engelmann, 1966; Kennel & Petschek, 1966) that is applicable to broadband, low amplitude waves (see discussion of its applicability in, e.g., Karpman, 1974; Shapiro & Sagdeev, 1997). The natural inhomogeneity of the background magnetic field in the Earth's magnetosphere relaxes the requirement of a broad wave spectrum (e.g., see discussion in Albert, 2001, 2010; Shklyar, 1981), but for a very high wave intensity the quasi-linear approach often becomes inaccurate (Allanson et al., 2020; Tao, Bortnik, et al., 2011; Tao et al., 2012; Wang et al., 2017). Indeed, a significant fraction of observed EMIC waves (Blum et al., 2016, 2017) and whistler waves (Cattell et al., 2008; Zhang et al., 2018; Zhang, Mourenas, et al., 2019) have sufficiently high amplitudes to resonantly interact with electrons nonlinearly (Albert et al., 2013; Artemyev et al., 2018; Shklyar & Matsumoto, 2009). Such nonlinear resonant interactions include two main effects: phase bunching (e.g., Albert, 2000, 2002; Artemyev et al., 2014) that results in electron non-diffusive drift in energy and pitch-angle space, and phase trapping (e.g., Demekhov et al., 2006; Omura et al., 2007) that results in large electron jumps in the same space. A fine balance between phase trapping and phase bunching (Artemyev et al., 2016; Shklyar, 2011; Vainchtein et al., 2018) provides a very fast electron flux evolution in systems with nonlinear resonances (Artemyev et al., 2021; Hsieh & Omura, 2017a, 2017b; Omura et al., 2015). For electromagnetic whistlers (propagating almost along the background magnetic field), phase trapping provides a fast electron acceleration (Bortnik et al., 2008; Furuya et al., 2008; Hsieh et al., 2020; Yoon et al., 2013), whereas phase bunching provides electron pitch-angle drift toward the loss-cone (Allanson et al., 2021; Artemyev et al., 2015; Bortnik et al., 2008; Hsieh et al., 2021; Mourenas, Artemyev, Agapitov, et al., 2016). For EMIC waves, phase trapping provides a strong decrease of electron pitch-angles (Grach & Demekhov, 2020; Grach et al., 2021; Kubota et al., 2015; Kubota & Omura, 2017), whereas phase bunching provides electron pitch-angle drift away from the loss-cone (Albert & Bortnik, 2009; Grach & Demekhov, 2018, 2020).

There are two possible scenarios of electron nonlinear resonant interactions with both whistler and EMIC waves. In the first scenario (already mentioned above), relativistic electrons can drift via phase bunching by whistler waves to smaller pitch-angles, where they can be trapped (or diffusion-like scattered) by EMIC waves and transported to the loss-cone. This scenario assumes that there are initially sufficient fluxes of relativistic electrons and that energy loss via phase bunching by whistler waves still keeps electrons within the range of energies resonant with EMIC waves. In the second scenario, high-energy (but not so high as to resonate with EMIC waves) electrons are trapped and accelerated by whistler waves until they can reach cyclotron resonance with EMIC waves, which then trap electrons and transport (or scatter in diffusion regime) them toward the loss-cone. The second scenario does not require initially high fluxes of relativistic electrons, but instead describes EMIC wave-driven precipitation of relativistic electrons previously accelerated locally by whistler waves. Both these scenarios are examined further in the present study.

Although for whistler waves the applicability of the cold plasma dispersion relation is well justified (at least as long as waves propagate quasi-parallel to the background magnetic field and do not approach the resonance cone angle, see discussions in Ma et al., 2017; Mourenas, Artemyev, Agapitov, & Krasnoselskikh, 2014), the same is not true for EMIC waves generated by energetic protons. Hot plasma effects in the EMIC wave dispersion relation may potentially increase or decrease the wavenumber that determines the minimum energies of resonant electrons (Silin et al., 2011). For the most intense EMIC waves, hot plasma effects decrease the wavenumber (thereby increasing the electron minimum energy [see Cao et al., 2017; Chen et al., 2019]). Therefore, the investigation of combined whistler and EMIC wave resonant interactions with electrons requires a thorough consideration of hot plasma effects for EMIC waves. This is also addressed in the current study.

To be diffused by whistler and EMIC waves, the electron can resonate with these two wave modes within two spatially separated regions. As scattering is a slow process, electrons may make several azimuthal rotations around the Earth before being moved to the loss-cone and, thus, they can resonate with whistler and EMIC waves at different local times (Mourenas, Artemyev, Ma, et al., 2016; Shprits et al., 2009; Zhang et al., 2017), and such spatially separated resonances do not reduce the rate of electron losses, because this rate is still lower than the time-scale of azimuthal drift. In the case of nonlinear resonant interactions, however, the presence of

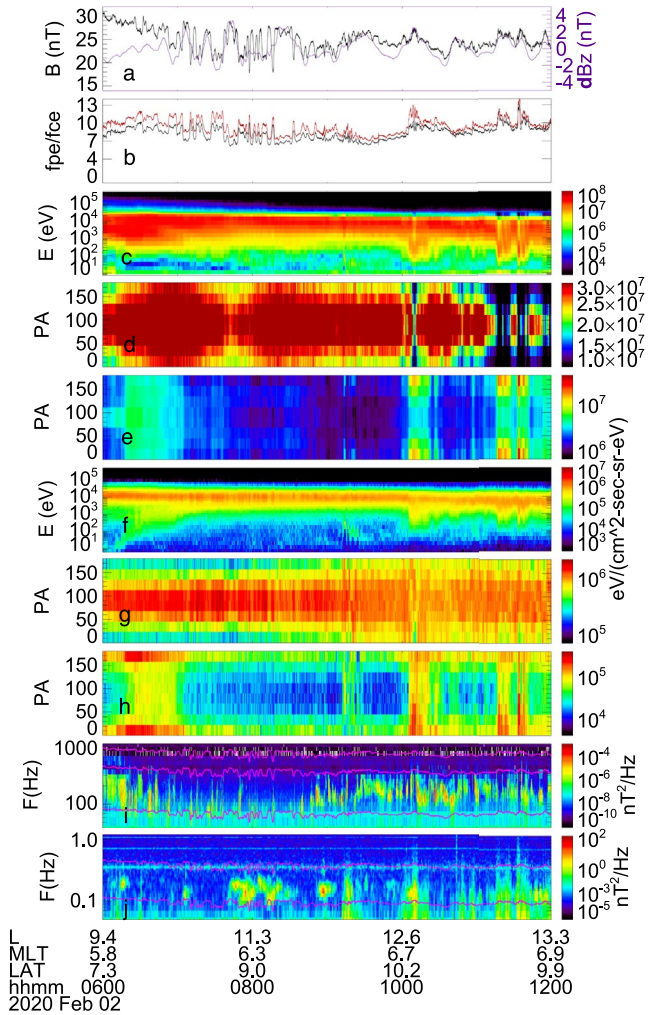

Figure 1. The overview of THEMIS-A observations on 2020-02-02 from 06:00 to 12:00: (a) total magnetic field (left axis) and $\delta B_{\parallel}$ (right axis), (b) f_{pe}/f_{ce} ratio for total (black) and equatorial magnetic field values, (c) omni-directional spectrum of electrons, (d and e) pitch-angle distributions of 5–10 keV and 5 eV–1 keV electrons, (f) omni-directional spectrum of ions, and (g and h) pitch-angle distributions of 5–10 keV and 5 eV to 1 keV ions. (i) *fff* magnetic field spectrum with f_{ce}, $f_{ce}/2$, and $f_{ce}/10$ shown by magenta curves and (j) magnetic field spectrum for EMIC wave frequency range f_{cp} and f_{cHe} shown by magenta curves.

both wave modes within the same spatial region may significantly speed up losses, because the nonlinear scattering is sufficiently strong to move electrons into loss-cone within a MLT-localized region. Therefore, the consideration of simultaneous electron resonances with both wave modes is more important for nonlinear resonances, than for slow diffusive scattering. The classical mechanisms of whistler and EMIC waves generation usually do not require these two waves modes to be observed simultaneously at the same local time (Shprits et al., 2006; Thorne, 2010): whistler waves are generated at the dawn flank by plasma sheet electrons drifting eastward (e.g., Tao, Thorne, et al., 2011), whereas EMIC waves are generated at the dusk flank by plasma sheet ions drifting westward (e.g., Blum et al., 2009; Jun et al., 2019). Therefore, to investigate the combined effects of nonlinear resonant interactions of electrons with whistler and EMIC waves, we should also consider the typical conditions for wave generation, for example, a local plasma compression that would result in ion and electron anisotropies responsible for such simultaneous EMIC and whistler wave generation (Gail & Inan, 1990; Remya et al., 2015; Yahnin et al., 2020). A potential candidate for such conditions is wave generation by plasma compressional modulation by ultra-low-frequency (ULF) waves. This modulation creates local maxima of ion and electron anisotropy, and may drive the simultaneous generation of whistler and EMIC waves (Kitamura et al., 2021; W. Li, Thorne, et al., 2011; Xia et al., 2016). Such intense compressional ULF waves around the flank of the magnetopause have been already reported to create intense whistler emissions (Zhang, Chen, et al., 2019; Zhang et al., 2020). Thus, in this study, we focus on such events encompassing ULF wave modulating whistler and EMIC waves.

We analyze in detail one such event observed by the Time History of Events and Macroscale Interactions during Substorms (THEMIS) mission (Angelopoulos, 2008). Section 2 describes the dataset and spacecraft instruments. We intend to use wave characteristics and cold plasma dispersion relation as input parameters to a test-particle simulation of electron interactions with whistler waves. Electron resonance with EMIC waves, however, is more affected by hot plasma dispersion effects. Thus, we first analyze the EMIC wave dispersion for the observed ion and wave characteristics in Section 3. The combined effects of electron resonant interaction with whistler and EMIC waves are investigated in Section 4, where we show the results of our test particle simulations. Then we discuss the obtained patterns of electron precipitations and the role of nonlinear resonant interactions in Section 5. The main results are summarized in Section 6.

2. THEMIS Observations: Datasets and Instruments

We analyze THEMIS A observations at the dawn flank ($MLT \sim 6.5$) on 2020-02-20 06:00–12:00 UT. During this time interval, THEMIS A moved from the lower L-shell toward the magnetopause ($L \in [9, 13]$) and observed compressional ULF waves. Figure 1a shows background magnetic field magnitude and the compressional ULF field component (frequency 2.5 mHz < f < 20mHZ). We use 1/5s resolution magnetic field data measured by the THEMIS fluxgate magnetometer (Auster et al., 2008). The background plasma density is ~ 1 cm^{-3}, and its variations anti-correlate with magnetic field variations. Therefore there are strong peaks of the plasma frequency to gyrofrequency ratio (f_{pe}/f_{ce}; see Figure 1b), a parameter playing a crucial role for wave-particle resonant interactions. Note to compute f_{pe}/f_{ce}, we only use the equatorial magnetic field (i.e., only the locally measured GSM B_z component), but this ratio is quite close to the one determined from the total magnetic field because THEMIS A was near the equator at the time (as typically, thanks to its orbit design). The plasma density in f_{pe} is obtained from electron measurements by the THEMIS electrostatic analyzer (McFadden et al., 2008) covering the energy range

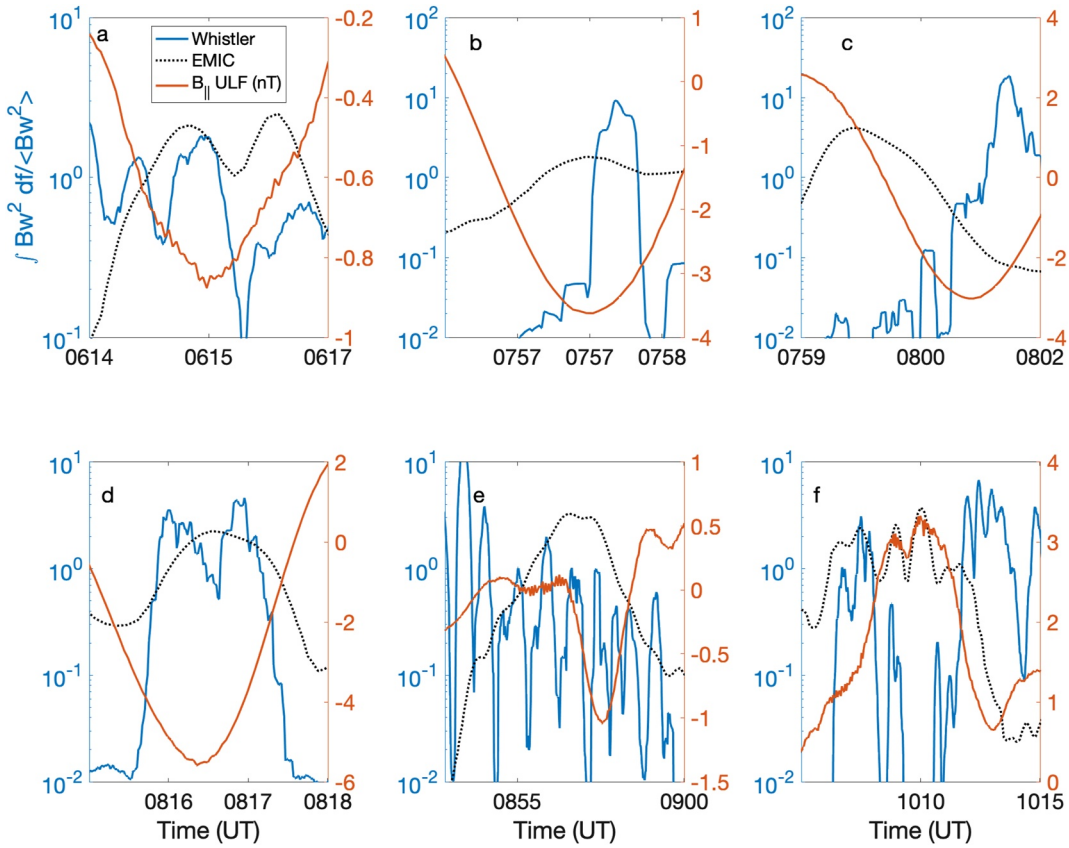

Figure 2. Six sub-intervals from Figure 1: each subinterval shows $\delta B_{\|}$ of ULF wave and normalized intensities of whistler and EMIC waves.

5 eV–25 keV, representing the main plasma component at these radial distances. We have verified these density measurements with estimates obtained from the spacecraft potential (Bonnell et al., 2008; Nishimura et al., 2013).

Figures 1c and 1f show electron and ion energy spectra collected by combined measurements of the electrostatic analyzer and solid-state telescope (Angelopoulos et al., 2008; Runov et al., 2015) over the energy range from 5 eV to 500 keV. The main electron and ion populations are below 50 keV. Electron and ion pitch-angle distributions for 5 keV < E <10 keV and E < 1 keV (Figures 1d and 1e for electrons and Figures 1g and 1h for ions) show a quasi-periodic modulation of the 90° anisotropy by the ULF wave compressions, that is, variations of these distributions are correlated with ULF wave activity (see quasi-periodic dynamics of ion and electron fluxes in Figure 1 and zoom-in subintervals in Figures S1 and S4 of Supporting Information S1). Such anisotropy peaks have been previously shown to correspond to hot particles trapped within magnetic field minima (Zhang, Chen, et al., 2019). The ion and electron populations generate intense whistler and EMIC waves, which are also seen in our event in magnetic field spectra for two frequency ranges, around hundreds of hertz in Figure 1i and hundreds of megahertz in Figure 1j. The whistler wave spectrum for frequency ∈ [30, 2,000] Hz is calculated on-board THEMIS (Cully et al., 2008) from THEMIS search-coil measurements (Le Contel et al., 2008) whereas the EMIC wave spectrum at frequencies < 2 Hz is calculated from fluxgate magnetic field measurements. Both whistler and EMIC wave emissions show quasi-periodicity that appears to be correlated with the wave intensity peaks around the local minima of the background magnetic field. To demonstrate this effect we select six sub-intervals with ULF $\delta B_{\|}$ minima. Figure 2 shows that such minima are associated with the enhanced intensities of whistler-mode and EMIC waves. The absence of one-to-one correlation between ULF, EMIC, and whistler-mode waves is most likely because we use the same frequency range for $\delta B_{\|}$ during all intervals, whereas the frequency of ULF waves modulating whistler and EMIC wave generation (Kitamura et al., 2021; W. Li, Thorne, et al., 2011; Xia et al., 2016) can vary with time. However, many bursts (or groups of bursts) of whistler and EMIC waves are observed within local $\delta B_{\|}$ minima.

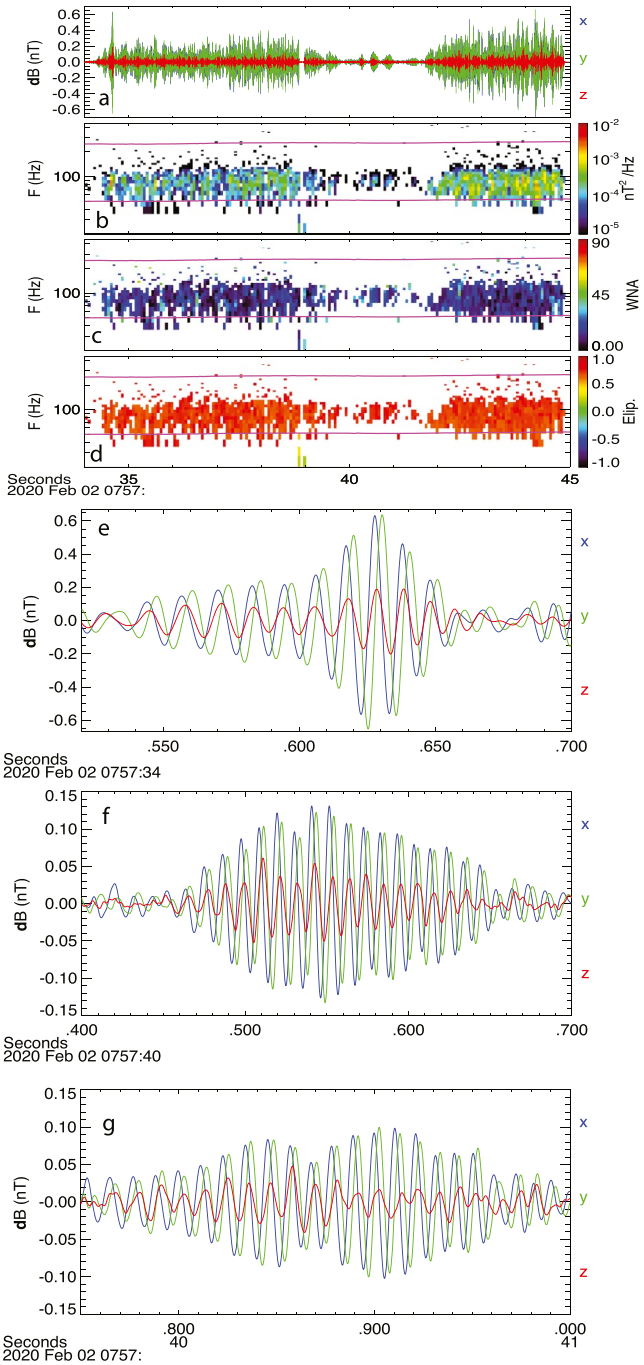

Figure 3. Whistler wave characteristics for a sub-interval of wave-form measurements: three components of whistler wave forms (a) shown in the field-aligned coordinate system (blue and green show two transverse magnetic field components, and red shows the field-aligned component), wave magnetic field spectrum (b), wave normal angle (c), and wave ellipticity (d). The two over-plotted magenta lines represent the frequency of $f_{ce}/2$ and $f_{ce}/10$. The instances of whistler wave packets in the field-aligned coordinates are shown in (e–g). Blue and green show two transverse magnetic field components, and red shows the field-aligned component.

Figure 3 zooms into several seconds of THEMIS search-coil measurements of whistler waveforms. Figure 3a shows that whistler waves propagate in the form of long packets with wave amplitude $\sim 100-300$ pT. These are quite intense whistler waves (compare with, e.g., statistics in W. Li, Bortnik, et al., 2011; Zhang et al., 2018). The observed whistler waves propagate along the background magnetic field (Figure 3c) with circular polarization (Figure 3d). Such waves are not affected by Landau resonance with suprathermal electrons and their dispersion is well described by cold plasma theory (Sazhin, 1993).

Figure 4 zooms in on ~ 1 hour interval of Figure 1 with observations of intense EMIC waves. The peak wave power is bracketed by the proton and helium gyrofrequencies (Figure 4b). The observed waves propagate quasi-parallel to the background magnetic field (Figure 4c) and their amplitudes reach ~0.5–1 nT, that is, these are intense hydrogen-band EMIC waves (see Zhang, Li, Thorne, et al., 2016).

In contrast to whistler waves, the EMIC wave dispersion may be significantly altered by the effects of hot anisotropic ions (Silin et al., 2011). To further analyze the EMIC wave properties and the associated ion contributions, we examine the linear wave growth model for the observed ion distribution functions averaged over three-time intervals when parallel propagating EMIC waves were observed. Figure 5 shows perpendicular (pitch-angles $\in [70°, 110°]$) and parallel (pitch-angles $\in [0°, 20°]$ and $\in [160°, 180°]$) phase-space densities of ions measured by the THEMIS electrostatic analyzer (McFadden et al., 2008). This instrument does not resolve ion species, and we assume that all measured fluxes are proton fluxes. This is a quite reasonable assumption for such large radial distances and is confirmed by the very close values of total ion and electron densities obtained from THEMIS electrostatic analyzer measurements. This suggests that the relative abundance of He+ is rather small and likely does not play a role in wave growth. Therefore, we fit the phase space density (PSD) profiles with a sum of three Gaussian proton distributions as shown in Figure 5. All three intervals are fitted with three (cold, warm, and hot) populations and the best-fit parameters are shown inside each panel of Figure 5.

3. EMIC Waves Dispersion

The dispersion relation for parallel propagating EMIC waves in a warm anisotropic plasma consisting of cold electrons, and cold, warm, and hot protons (following Chen et al., 2011) can be written as

$$\begin{aligned} y^2 \;=\; & \frac{x^2}{f^2}\frac{m_e}{m_p} - x + (1-\eta_{wp}-\eta_{hp})\frac{x}{1-x} \\ & +\eta_{wp}\left[A_{wp} + \left(A_{wp} + \frac{x}{x-1}\right)\xi_{wp}\mathcal{Z}(\xi_{wp})\right] \\ & +\eta_{hp}\left[A_{hp} + \left(A_{hp} + \frac{x}{x-1}\right)\xi_{hp}\mathcal{Z}(\xi_{hp})\right] \end{aligned} \tag{1}$$

where $x = \omega/\Omega_p = \Re\omega/\Omega_p + i\gamma/\Omega_p$ is the normalized complex frequency, $\omega_{(pi,pe)} = \sqrt{n_{0e}e^2/(\epsilon_0(m_e,m_p))}$ and $\Omega_{(e,p)} = eB_0/m_{(e,p)}$ are the plasma frequency and gyro frequency for electrons and protons respectively, $y = ck/\omega_{pi}$ is the normalized field-aligned wavenumber, c is the speed of light, and $f = \omega_{pe}/\Omega_{ce}$ represents the electron plasma frequency to gyro frequency ratio. The

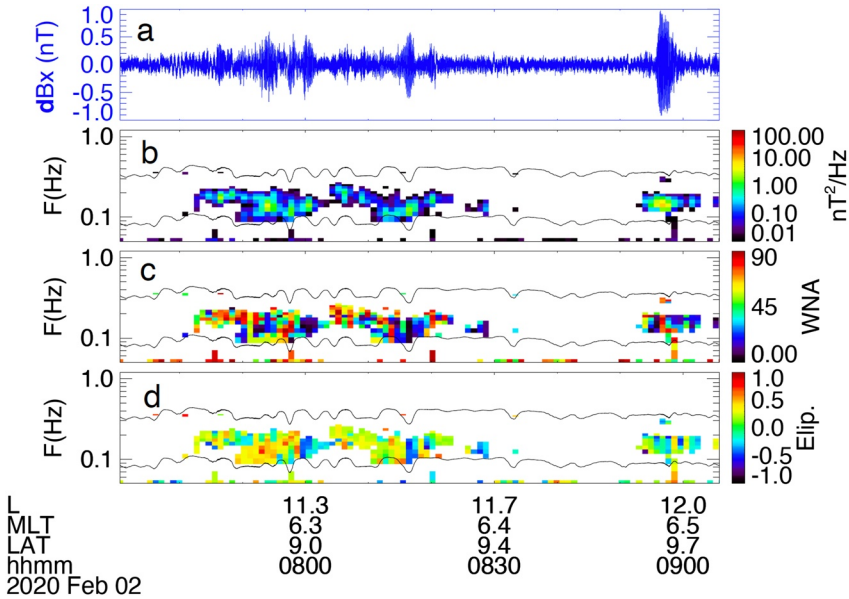

Figure 4. EMIC wave characteristics for sub-interval with high wave intensity: one component of EMIC wave form (a), wave magnetic field spectrum (b), wave normal angle (c), and wave ellipticity (d). Two horizontal black curves show f_{cHe} and f_{cp} frequencies.

fractional composition of warm and hot protons are defined as $\eta_{wp} = n_{wp}/n_e$ and $\eta_{hp} = n_{hp}/n_e$, respectively, where n_{0e} is the electron density which satisfies the quasi-neutrality condition ($n_{0e} = n_{cp} + n_{wp} + n_{hp}$). $\mathcal{Z}$ is the usual plasma dispersion function (Fried & Conte, 1961) with argument $\xi_{(wp,hp)} = (x-1)/(y\sqrt{2T_{(wp,hp)\|}/m_p}/v_A)$ where $v_A = B_0/\sqrt{\mu_0 m_p n_{0e}}$ is the Alfven speed. The factor $A_{(wp,hp)} = T_{(wp,hp)\perp}/T_{(wp,hp)\|} - 1$ is the temperature anisotropy.

In these dimensionless variables, the minimum resonant energy of electrons resonating with EMIC waves is given by

$$E_{\min} = \left(\sqrt{1 + \frac{m_p}{m_e}\frac{1}{f^2 y^2}} - 1\right) m_0 c^2 \tag{2}$$

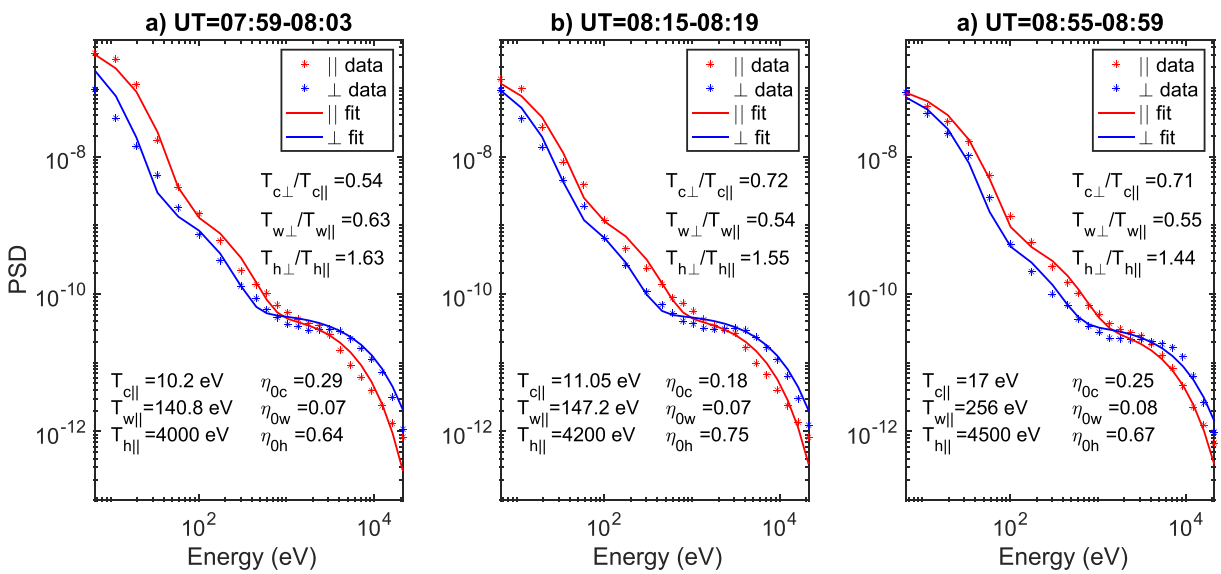

Figure 5. Three examples of profiles of ion parallel and perpendicular phase space density. The parallel and perpendicular components are shown by red and blue colors, respectively, with curves (solid lines) showing fittings of observed data (dots). Time intervals of data averaging are indicated above each panel. The proton density, parallel temperature, and anisotropy ($T_\perp/T_\parallel$) of cold, warm, and hot populations are denoted by subscripts c, w, and h, respectively.

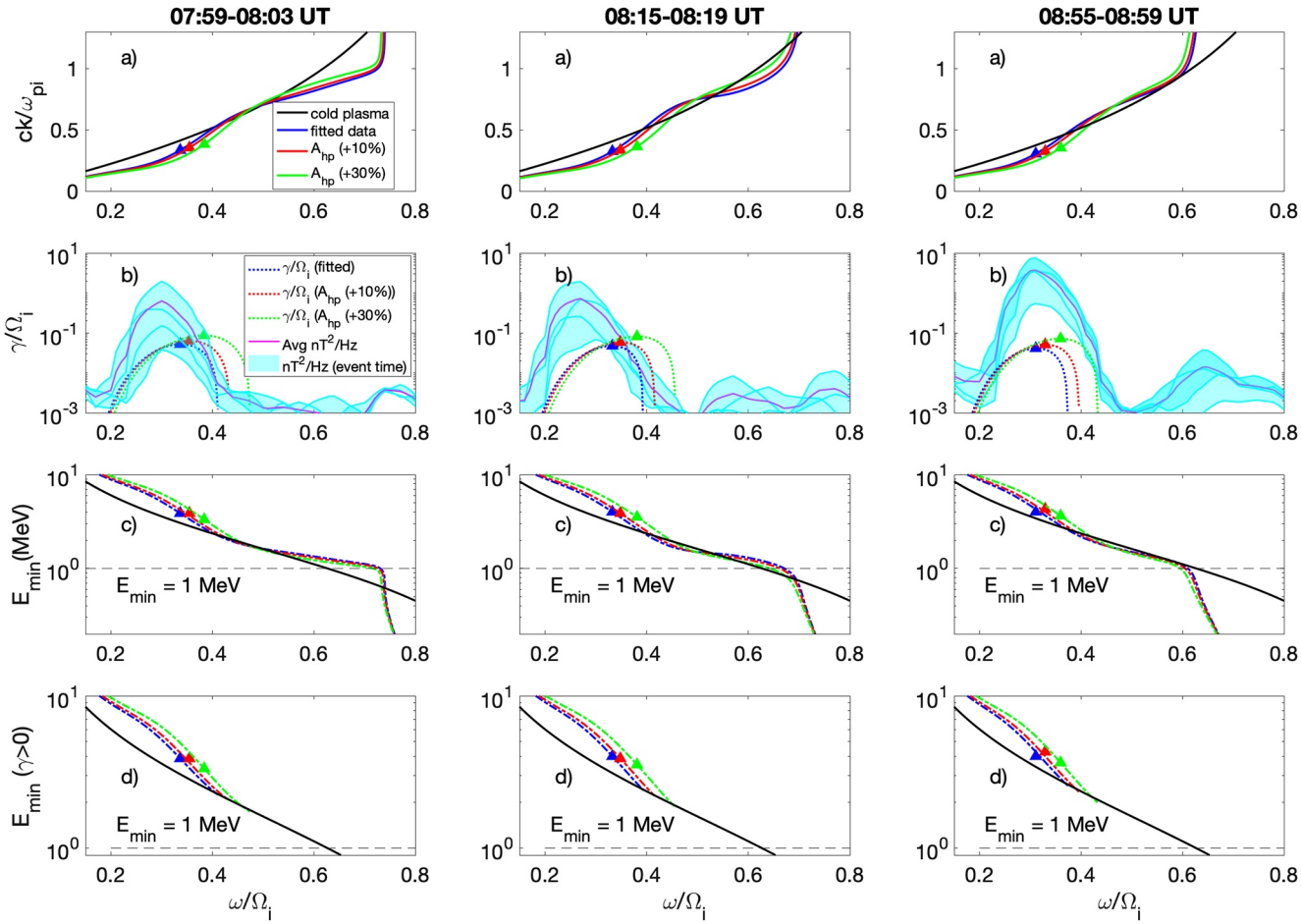

Figure 6. EMIC wave dispersion relations for three ion distributions are shown in Figure 5. From top to bottom: (a) ω(k) dispersion curves, (b) $\gamma(\omega)$ wave growth rates with over-plotted averaged power spectral density of observed EMIC wave during the time periods mentioned above the top panels (we show several individual spectra and a range of intensity/frequency covered by observed waves [cyan shades]), (c) $E_{\min}(\omega)$ minimum energy of electrons resonating with EMIC waves, and (d) $E_{\min}$ for positive growth rate (i.e., $\gamma > 0$) only. Black curves show cold plasma dispersion, colors show different levels of ion anisotropy ($A_{hp} = T_{h\perp}/T_{h\|}$) for the fitted data (blue), 10% increased A_{hp} (red), and 10% increased A_{hp} (green). Triangles indicate the instances of maximum growth rate.

For fixed wave frequency, this equation shows that a larger wavenumber corresponds to smaller energies of electrons resonating with EMIC waves.

We fit the observations with three populations of protons each a Gaussian (see the comparison of observational and fitted distributions in Figure 5) to the set of parameters of Equation 1. Next, we numerically solve the parallel propagating EMIC wave dispersion relation (Equation 1), and present the results of these calculations in three columns of Figure 6 (blue curves). The crucial parameter for EMIC wave dispersion, the ion temperature anisotropy, $A_{(wp,hp)}$, can be underestimated from the distribution fitting because: (a) the real anisotropy can be more localized around ~90° pitch-angles and be smoothed by pitch-angle averaging and our Gaussian fits; (b) the measured anisotropy can correspond to an already relaxed ion distribution after it has lost some fraction of its initial free energy due to feedback of the waves on the distribution. Therefore, we also provide the results for 10% (red curves) and 30% (green curves) greater anisotropy compared to the best fit to the observations (blue curve). The cold plasma dispersion solution for the observed electron plasma frequency to gyro frequency ratio ($f = 15$) is also shown as black curves.

The comparison of the hot and cold plasma dispersion relations in Figure 6a indicates that hot plasma effects can change the normalized wavenumber significantly. In the lower frequency range, the wavenumber is smaller in the hot plasma case than for cold plasma, as expected. However, as frequency increases, the wavenumber tends to increase and then approaches the cold plasma solution, or even slightly exceeds it. Different sets of fitting

parameters for the three intervals exhibit different wavenumber profiles, but the general trend is that the wavenumber from the hot dispersion increases with frequency faster than the cold dispersion wavenumber. If we limit our discussion only to the frequency range corresponding to positive growth rates (i.e., $\gamma > 0$), we obtain that the largest hot dispersion wavenumber is the same as the cold plasma one for the first instance (left Figure 6a), whereas it is larger than the cold plasma wavenumber in the other two cases (middle and right Figure 6a).

The estimated growth rates (Figure 6a) obtained by using the fitting parameters are in good agreement with the observed power spectral density, that is, we observe the most intense waves within the frequency range where wave growth ($\gamma > 0$) is expected. The comparison of Figures 6a and 6b shows that the strongest waves (corresponding to the highest growth rate) have wavenumber smaller than cold plasma wavenumber, and this agrees with previous results that the minimum resonant energy increases due to hot plasma effects (Cao et al., 2017; Chen et al., 2019). However, the higher frequency range (with smaller wave intensity, but still $\gamma > 0$) corresponds to a slight increase of the wavenumber compared to cold plasma values, and such EMIC waves may resonate with electrons having slightly smaller energies. To confirm this, we show $E_{\min}$ for calculated hot and cold plasma dispersion relations (see Figure 6d where $E_{\min}$ for the hot plasma dispersion is shown only for frequencies such that $\gamma > 0$). There is a clear effect of $E_{\min}$ in the hot plasma case reaching the cold plasma $E_{\min}$ and even going slightly below this limit. Thus, for the investigation of resonant interactions of not-so-high energy electrons with EMIC waves, we shall consider the low-amplitude, higher-frequency part of the observed wave spectrum.

Figure 6 shows that although $\gamma > 0$ frequency range is quite close to the range of observed intense EMIC waves, there is a finite wave power at $\omega/\Omega_i > 0.5$ where we have $\gamma < 0$ for our model. As such higher frequency part of the wave spectrum can be the most important one for the scattering of lower energy electrons, we modify the ion distribution fittings to reproduce $\gamma > 0$ at $\omega/\Omega_i > 0.5$ (one example shown in Figure 5a has been examined). There are two approaches to get $\gamma > 0$ at a higher frequency range. We have verified that both approaches for all three intervals from Figure 5 lead to almost the same results. Thus, we illustrate these approaches for one of these three intervals, 07:59–08:03 UT. The first approach assumes that our fit of ion distribution underestimates the anisotropy and/or density of the warm ion population. The introducing an additional warm ion population with sufficiently high anisotropy we can cover the wider frequency range with $\gamma > 0$ (compare Figures 7b and 7f). However, the contribution of such warm ion population to the EMIC wave dispersion decreases the wavenumber for $\omega/\Omega_i > 0.5$ (and increases the minimum resonant energy). Moreover, the energy range of the warm ion population $\sim$[0.1, 1] keV is well covered by THEMIS measurements, and we unlikely underestimate this population by the fittings shown in Figure 5. The second approach suggests that there is a hot ion population with sufficiently high anisotropy. The contribution of this population to the EMIC wave dispersion significantly alters the frequency range of the positive growth rate (compare Figure 7b and Figure 7j) and reduces the minimum resonant energy (compare Figure 7d and Figure 7l). An important property of this population is that it may have a transient nature and not be present for the entire time interval of EMIC wave generation, because the high-frequency part of the EMIC spectrum is quite transient (see Figure 6b for individual profiles of EMIC spectra during different intervals). Such transient nature of high-frequency EMIC wave generation suggests that most of the time we observe stably generated EMIC waves with $\omega/\Omega_i < 0.5$ (the main part of the time-averaged EMIC spectrum, see Figure 7b), whereas the small occurrence rate of high-frequency EMIC waves results in weak wave intensity at $\omega/\Omega_i > 0.5$. Due to large anisotropy, the energy range of this hot population is partially beyond the THEMIS electrostatic analyzer and should be covered by a solid-state telescope (Angelopoulos et al., 2008) with not-so-good pitch-angle resolution. Taking into account the required transient nature of this population, we may underestimate its density and anisotropy for THEMIS measurements, that is, the existence of such a free energy source for EMIC waves does not contradict THEMIS plasma measurements and is supported by observed EMIC spectra. Similarly, the highest frequency EMIC waves near $0.8f_{cp}$ in Figures 6 and 7 are probably generated by another transient proton population with $T_{\parallel} \sim$ 2–20 eV and $T_{\perp} \sim$ 50–500 eV (Min et al., 2021; Teng et al., 2019), the transient nature of this population similarly preventing its identification in THEMIS 3-s plasma measurements. Although we will use mostly cold plasma dispersion of EMIC waves for simulations of electron resonant scattering, we will also check hot plasma effects for the reduction of the minimum resonant energy.

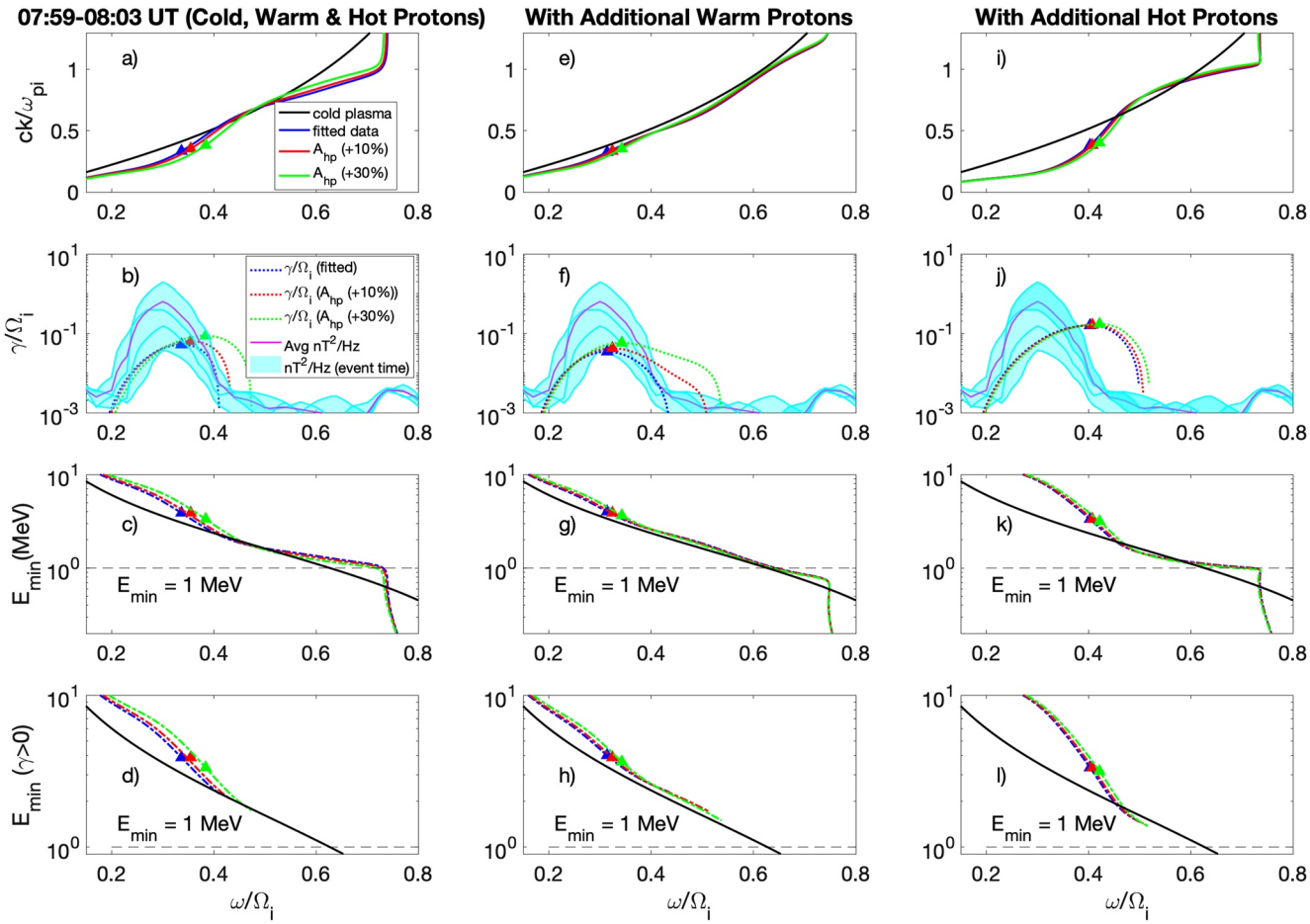

Figure 7. EMIC wave dispersion relations for ion distribution shown in Figure 5a. From top to bottom, a–d represents exactly the same results for three (cold, warm, and hot) proton populations as that of a–d of 07:59-08:03 UT case in Figure 6. Panels (e–h) depict the results of an additional warm proton (represented by subscript *wp*2), population whereas i–l are for an additional hot proton population (represented by subscript *hp*2). For additional warm proton population case, we use $\eta_{hp} = \eta_{wp2} = 0.32$, $T_{wp2} = 340$ eV and $T_{wp2\perp}/T_{wp2\parallel} = 1.52$, and for additional hot proton case we use $\eta_{hp} = \eta_{hp2} = 0.32$, $T_{hp2} = 8{,}000$ eV and $T_{hp2\perp}/T_{hp2\parallel} = 3.5$.

4. Electron Precipitation Patterns

To investigate electron losses due to the combined effects of whistler and EMIC waves, we perform a series of test particle simulations. The simulation scheme is based on Hamiltonian equations for a monochromatic wave (see Artemyev et al., 2021; Vainchtein et al., 2018), that is, we consider one whistler wave and one EMIC wave with the typical observed characteristics. The background magnetic field is given by a curvature-free dipole model (Bell, 1984) with the equatorial value $B_{0,eq} = 21$ nT and inhomogeneity scale $R = 11.5R_E$ (for the field-aligned coordinate, we use the dipole magnetic latitude, λ). This field sets the equatorial gyrofrequency $f_{ce,eq}$, whereas the plasma frequency f_{pe} is taken from observations, $f_{pe}/f_{ce,eq} \simeq 7$–$14.5$. The time is normalized to a typical scale $R/c \approx 0.2$ s, with the one bounce period of relativistic elections being ~ 5 ($5\ R/c \sim 1$ s).

The whistler wave frequency is $f_{wh}/f_{ce,eq} = 0.35$, the observed wave amplitude is $B_{w,wh} = 200$ pT, and the wave dispersion relation $k_{wh} = k_{wh}(f_{wh}, \lambda)$ is given by the cold plasma dispersion for field-aligned whistler waves (Stix, 1962). We assume that waves are generated at the equator and their intensity decreases quickly at high latitudes (see statistics of whistler wave intensity distribution along magnetic field lines in, e.g., Agapitov et al., 2013, 2018; Wang et al., 2019). Thus, the whistler wave amplitude is $B_{w,wh} \to B_{w,wh} \cdot \Lambda(\lambda)$ with its latitudinal dependence modeled as: $\Lambda(\lambda) = 0.5 \cdot (1 + \tanh(\lambda/\delta\lambda_1)) \exp\left(-(\lambda/\delta\lambda_2)^2\right)$ and $\delta\lambda_{1,2} = 1°$ and $20°$. For waves generated at the equator and propagating to higher latitudes, the wave-particle resonant interaction is symmetric relative to the equator, and there are two resonances per bounce period for each electron: one resonance at $\lambda > 0$ and another at $\lambda < 0$. Function $\Lambda(\lambda)$ describes the wavefield distribution for $\lambda > 0$, whereas we do not include the resonance

at $\lambda < 0$. This simplifies the model description of wave-particle interaction, but does not alter the effects of such interaction (it only extends the time interval between two successive resonances from half of the bounce period to one bounce period).

In contrast to the modeling of the whistler-mode wave, for which we use the most intense wave from the observed spectrum, the EMIC wave frequency is taken as $f_{EMIC}/f_{cp,eq} = 0.55$, with a wave amplitude $B_{w,EMIC} = 200$ pT (i.e., we use a wave intensity ~1/25 times smaller than the peak intensity of observed waves with amplitudes of ~1 nT; see Figures 6b and 4). This is not the frequency of the most intense EMIC waves observed during the event under consideration. Instead, we use the mean value of the highest frequency of observed EMIC waves, which corresponds to the minimum resonant energy of electrons potentially interacting with EMIC waves: this energy is given by equation $E_{\min} = \left(\sqrt{1 + \Omega_e^2/c^2k_\parallel^2} - 1\right) m_0c^2$ (Denton et al., 2015; Summers & Thorne, 2003). For comparison we also model $f_{EMIC}/f_{cp,eq} = 0.5$ with the same wave amplitude. For the EMIC wave dispersion relation, we use the cold plasma dispersion $k_{EMIC} = k_{EMIC}(f_{EMIC}, \lambda)$ (Stix, 1962) and the dispersion corrected for hot plasma effects $k^*_{EMIC} = 1.3 \cdot k_{EMIC}(f_{EMIC}, \lambda)$ where $k^*_{EMIC}/k_{EMIC} = 1.3$ overestimates $k^*_{EMIC}/k_{EMIC} \approx 1.1$ from Figure 6, but allows us to examine the maximum possible effect of the hot plasma dispersion. This simplified form of hot plasma correction does not include changes of wavenumber variation with latitude due to hot plasma effects, but it allows to include hot plasma effects on electron resonant energy recalculation. Similar to whistler waves, we use a latitudinal distribution of EMIC waves as $B_{w,EMIC} \to B_{w,EMIC} \cdot \Lambda(\lambda)$ with $\Lambda(\lambda) = 0.5(\tanh(\lambda/\delta\lambda_1) - \tanh((\lambda - \delta\lambda_2)/\delta\lambda_1))$ with $\delta\lambda_{1,2} = 1°$ and 15°, that is, there is no EMIC wave anymore around and above the helium resonance latitude that is around ~25° for the chosen wave frequency. Note for EMIC waves we use the same simulation scheme with a single resonance per bounce period, as used for the whistler-mode wave.

ULF-modulated whistler-mode and EMIC waves show peak of intensity with a half of ULF period (with magnetic field minimum, see Figure 2), and almost disappear on the second half of the ULF period (with magnetic field maximum). Thus, the simulation time should be a half of the ULF period, that is about ~10 min. To model a sufficient number of electron trajectories we reduce this half of the ULF period interval to 600 $R/c \approx 2.5$ min. During this interval we modulate wave amplitudes, $B_{w,wh} \to B_{w,wh} \cdot U(t)$, $B_{w,EMIC} \to B_{w,EMIC} \cdot U(t)$, background magnetic field $B_0 \to B_0 \cdot (1 - a_1\dot{U}(t))$, and frequency ratio $f_{pe}/f_{ce,eq} \to \min(f_{pe}/f_{ce,eq}) \cdot (1 + a_2\dot{U}(t))$, where $\min(f_{pe}/f_{ce,eq}) = 7$, $U(t) = \sin(\pi \cdot t/600)$ (i.e., $B_{w,wh} = 0$ and $B_{w,EMIC} = 0$ at $t = 0$, 600). Parameters $a_1 = 0.12$ and $a_2 = 1.07$ are taken from the fitting of the observed magnetic field and plasma density.

Figure 8 shows several examples of test particle trajectories from this simulation (with cold plasma dispersion). We plot trajectories in energy versus equatorial pitch-angle space, and use colors to indicate the time of simulation, ct/R (see time series of electron energy and pitch-angle in Figures S3 and S4 of Supporting Information S1). Figure 8a shows two trajectories for initial energy $E = 50$ keV but different initial pitch-angles. Electrons of these energies do not reach cyclotron resonance with EMIC waves and only interact with whistler waves. Within ~100 − 200 resonant interactions, electrons cover a significant fraction of the pitch-angle range (from 50° to 5° for one trajectory; from 15° to 90° and then back to 50° for another trajectory). Pitch-angle time series (see Figures S3 and S4 in Supporting Information S1) confirm that such fast pitch-angle changes are due to phase bunching (electron pitch-angle decrease with a nonzero mean $\Delta\alpha_{eq}$) and phase trapping (very large positive $\Delta\alpha_{eq} \sim 60°$), therefore Figure 8 depicts clearly mostly nonlinear effects (see also $\Delta\alpha_{eq}$ distributions in Figure 9). Figure 9a shows that electron trajectories indeed consist of gradual drifts to smaller energy and pitch-angles (drift to the loss-cone due to the phase bunching), and a few large jumps to higher energies and pitch-angles (see also Figures S3 and S4 of Supporting Information S1). Trajectory starting with $\alpha_{eq} = 49°$ does not experience such a jump and directly drifts to the loss cone (the initial position in the energy, pitch-angle space is shown by a cross). The resonant interaction with monochromatic waves conserves the total energy in the wave reference frame, that is, the quantity $\gamma - (f_{wh}/f_{ce,eq})\mu$ remains an invariant with $\gamma = E/m_ec^2 + 1$ and $\mu = (\gamma^2 - 1)\sin^2\alpha_{eq}/2$ (Shklyar & Matsumoto, 2009). Conservation of this invariant shows that the pitch-angle change is much larger than the energy change for small energy electrons (γ close to one): $\Delta\alpha_{eq} \sim \Delta\gamma/(\gamma^2 - 1)$. This is why particles mostly drift along pitch-angle and change their energies insignificantly in the phase bunching regime shown in Figure 9a. The trajectory starting with $\alpha_{eq} = 15°$ (see the initial position in the energy, pitch-angle space shown by cross) shows a large acceleration (due to the phase trapping) to 110 keV accompanied by pitch-angle increase from the initial $\alpha_{eq} \sim 15°$ to almost 90°. After this acceleration due to trapping the electron drifts to smaller energy, pitch-angle, but does not reach the loss-cone within the simulation time. The similar behavior of two trajectories with initial energy 100 keV (too small to resonate with EMIC waves) can be seen in Figure 9b: one electron quickly drifts to

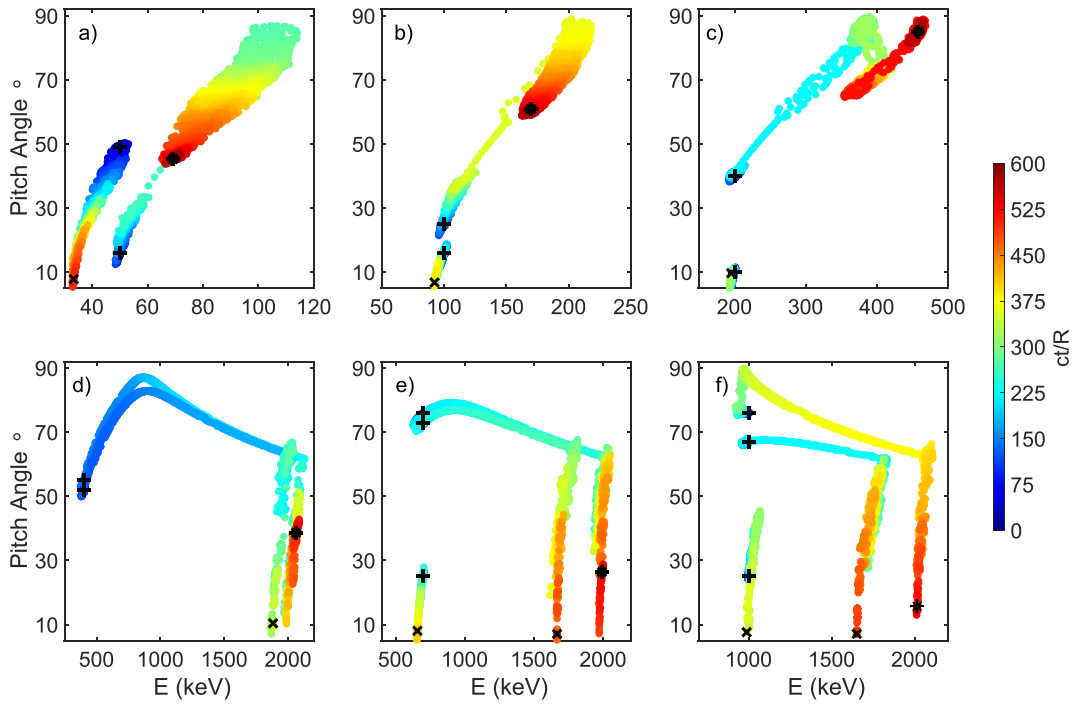

Figure 8. Pitch angle versus energy plots showing the trajectories due to the combined effect of whistler and EMIC waves, where the color bar shows the time evolution. The initial values of trajectories in (pitch angle and energy) space are represented by "+" sign. "*" denotes the values when the simulation ends for trapped particles, whereas "*x*" depicts the values when particles are scattered below $\alpha_{eq} < 5°$. The six panels are for six different initial energies: (a) 50 keV (initial $\alpha_{eq} = 15°$ and 49°), (b) 100 keV (initial $\alpha_{eq} = 16°$ and 25°), (c) 200 keV (initial $\alpha_{eq} = 10°$ and 40°), (d) 400 keV (initial $\alpha_{eq} = 52°$ and 55°), (e) 700 keV (initial $\alpha_{eq} = 25°$, 73°, and 76°), and (f) 1,000 keV (initial $\alpha_{eq} = 25°$, 67°, and 76°). *Note*. Time series of electron energy and pitch-angles for all shown trajectories can be found in Figures S3 and S4 of Supporting Information S1.

the loss-cone with a small energy decrease, and another electron is accelerated to 200 keV with the pitch-angle increase to ~90° (see also Figures S3 and S4 in Supporting Information S1).

Figure 8c also shows two trajectories of initial energy 200 keV not resonating with EMIC waves. The electron with a small initial pitch-angle quickly drifts to the loss-cone due to phase bunching by the whistler wave, whereas the electron with initial $\alpha_{eq} \sim 40°$ is trapped and accelerated by the whistler wave (see also Figures S3 and S4 in Supporting Information S1). Our simulation assumes a constant wave frequency, and thus both trapping and phase bunching should move electrons along the same resonant curve $\gamma - (f_{wh}/f_{ce,eq})\mu = \text{const}$, but the adiabatic modulation of magnetic field (i.e., $f_{ce,eq}$) modifies this curve: for example, the accelerated electron trajectory lies on two segments, each with $\gamma - (f_{wh}/f_{ce,eq})\mu = \text{const}$ but with different $f_{wh}/f_{ce,eq}$.

Figure 8d shows two electron trajectories with an initial energy of 400 keV. Although this energy is too small to reach cyclotron resonance with EMIC waves, trapping acceleration by whistler waves is quite different for this energy in comparison with the smaller initial energies shown in Figures 8a–8c. Trapped electrons start gaining energy with a simultaneous pitch-angle increase, as in the previous examples, but their acceleration is sufficiently effective to reach ~1 MeV. This is the threshold energy to drive the so-called turning acceleration (Omura et al., 2007; Summers & Omura, 2007) by whistler waves. Formally, trapped electrons remain in resonance, but their resonant momentum $p_{\parallel} = 2\pi(f_{wh}\gamma - f_{ce})/k$ changes direction, because γ becomes larger than f_{ce}/f_{wh}. Such a change of the direction of trapped particle motion allows these particles to stay longer within the resonance and gain even more energy. The final energies of accelerated electrons in Figure 8d are about 2 MeV. Around the time when γ reaches f_{ce}/f_{wh}, the trapped electron pitch-angles start decreasing, because for such energies $(f_{wh}/f_{ce,eq})(\gamma^2 - 1)/2$ grows faster than γ, and the pitch-angle should go down to satisfy $\gamma - (f_{wh}/f_{ce,eq})\mu = \text{const}$. Escaping from trapping with an energy ~2 MeV near $t = 300\ R/c$, at the time when the ULF wave-driven modulation creates the highest $f_{pe}/f_{ce,eq}$ value, electrons start interacting resonantly with the EMIC wave, if electron pitch-angles are not too large (the large pitch-angle electrons keep resonating with the whistler wave only until scattering on

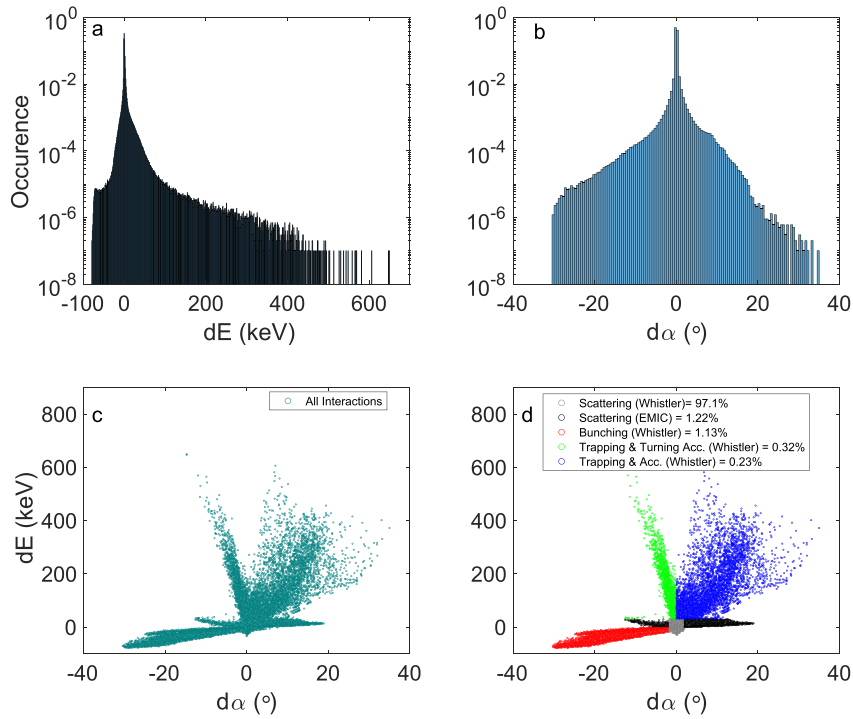

Figure 9. Distributions of energy (a) and pitch-angle (b) changes for a single resonant interaction ($\sim 10^7$ number of interactions are shown). The distribution of these changes for all interactions is depicted in (c) and colored accordingly to several mechanisms of wave-particle interactions (d; see text for details).

whistlers will not reduce electron pitch-angles to the range of resonances with EMIC waves). Electron resonant interaction with EMIC wave quickly scatters them to the loss-cone. This interaction is seen as an almost straight line $\gamma = \text{const}$ going from $\alpha_{eq} \sim 65°$ to the loss-cone, because resonance with EMIC wave does not change the energy significantly, whereas the whistler wave does not have sufficient time to change the electron energy during the electron's quick scattering by the EMIC wave. Note that during their resonant interaction with EMIC waves, electrons move along the resonant curve $\gamma + (f_{EMIC}/f_{ce,eq})\mu = \text{const}$ where the factor $f_{EMIC}/f_{ce,eq}$ is negligibly small, guaranteeing approximate energy conservation.

Figures 8e and 8f show electron resonant interactions with whistler and EMIC waves for the initial energies $\sim$700 keV and 1 MeV. The main feature of the results shown in Figure 8d is that such high initial energy leads to trapping electron acceleration in the turning regime (energy increase/pitch-angle decrease) almost from the beginning of trapping, that is, there are no trajectories with both energy and pitch-angle increase. After acceleration by whistler waves, these electrons start resonating with the EMIC wave that quickly scatters them to the loss-cone. Note the trapping acceleration is available mostly for electrons with sufficiently large initial pitch-angles, whereas electrons with initially small pitch-angles move to the loss-cone due to the phase bunching by whistler waves (see also Figures S3 and S4 in Supporting Information S1).

To characterize different resonant effects of electron interaction with intense whistler wave and moderate EMIC wave, we collect distributions of pitch-angle and energy changes for a single resonance (during a single bounce period) by numerically integrating over a large electron ensemble. Figure 9 shows that ΔE and $\Delta\alpha_{eq}$ distributions span over a large range with significant occurrence rates at $|\Delta E| > 50$ keV and $|\Delta\alpha_{eq}| > 10°$ for a single resonant interaction, that is, we deal with a non-diffusive regime of electron resonant interaction. We also plot the distribution in (ΔE, $\Delta\alpha_{eq}$) space, where four different populations can be well identified (note, to separate effects of resonance with whistler and EMIC waves we check the conservation of $\gamma - (f_{wh}/f_{ce,eq})\mu = \text{const}$ and $\gamma + (f_{EMIC}/f_{ce,eq})\mu = \text{const}$ for each shown pitch-angle and energy change). The blue population of (energy and pitch-angle) changes shows electrons experiencing the phase trapping by whistler wave (0.23% of all shown changes): energy and pitch-angle increase due to such trapping. The green population shows the same phase trapping, but with the turning acceleration (0.32% of all shown changes): energy increase of such electrons are associated with

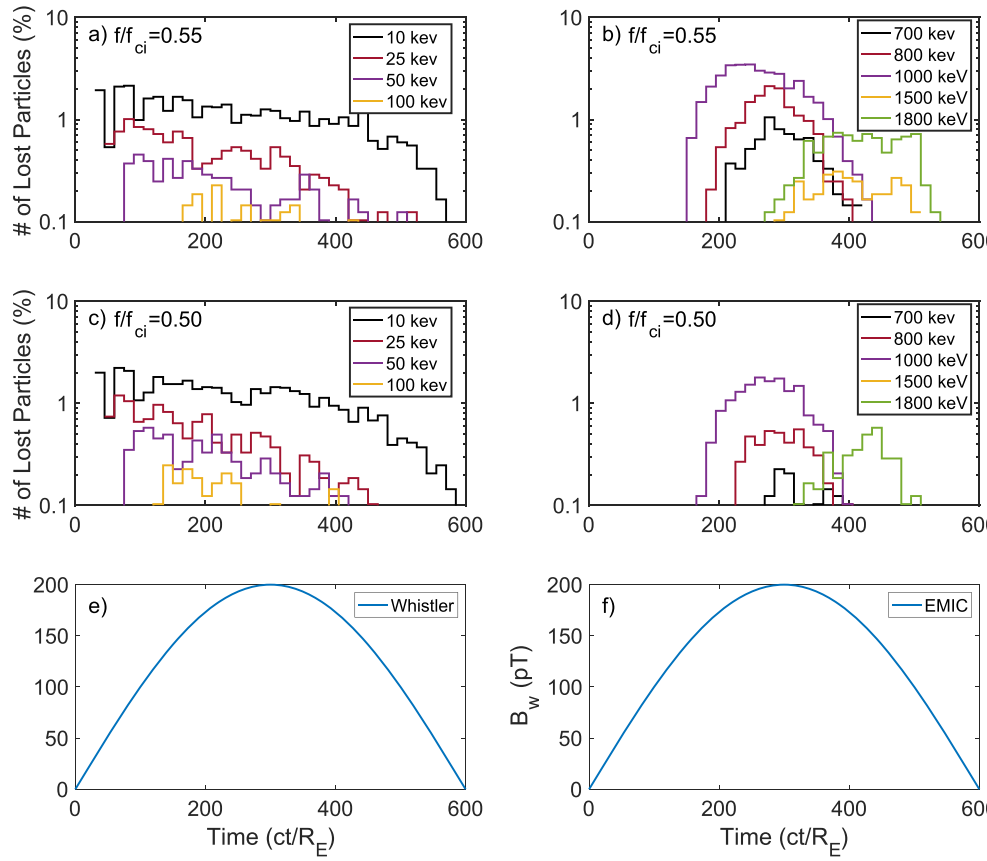

Figure 10. Percentage of electrons scattered below $\alpha_{eq} < 5°$ for a system with EMIC and whistler waves, where colors show different energies. The results for EMIC frequency $f/f_{cp} = 0.55$ are shown in (a and b) and for $f/f_{cp} = 0.50$ in (c and d). Bottom panels show time profiles of wave intensities.

pitch-angle decrease (see Omura et al., 2007 and pitch-angle, energy time series in Supporting Information S1). The red population shows electrons experiencing the phase bunching by whistler-mode waves (1.13% of all shown changes): energy and pitch-angle decrease, and $|\Delta E|$ due to bunching is significantly smaller than $|\Delta E|$ due to trapping. The black population shows electrons resonating with EMIC waves: a significant pitch-angle change without significant energy variations (1.22% of all shown changes). As this interaction is characterized by comparable positive and negative $\Delta\alpha_{eq}$, this is likely diffusive scattering by EMIC wave with an amplitude insufficient for nonlinear resonant interactions. We also use the gray color for the population of electrons with $|\Delta E| < 30$ keV and $|\Delta\alpha_{eq}| < 2°$ (97.1% of all shown changes): these electrons are most likely diffusively scattered by the whistler wave or non-resonantly interact with EMIC waves (Chen et al., 2016).

To generalize results shown for individual trajectories in Figure 8, we numerically integrate an ensemble of 1.65×10^5 trajectories. We use 34 initial energy values (from 10 to 1,050 keV) and for each energy, we use a uniform initial pitch-angle distribution (from 10° to 76°) to calculate the percentage of particles scattered to $\alpha_{eq} < 5°$ at each time step. This boundary pitch-angle is larger than the real loss-cone pitch-angle $\alpha_{LC} \sim 1°$–$2°$ at $L \sim 12$ of spacecraft observations shown above, but there is almost no energy change for particles between $\alpha_{eq} \sim 5°$ and 1° for cyclotron resonance with whistler and EMIC waves, that is, energy distributions of electrons with $\alpha_{eq} < 5°$ would be very similar to the energy distributions of lost electrons. Figure 10 shows time-series of the percentage of electrons with $\alpha_{eq} < 5°$ (note that when a trajectory crosses this pitch-angle, we stop integration and consider this electron as lost, i.e., each electron can contribute only once to the distribution in Figure 10). The magnitude of percentages of electrons crossing $\alpha_{eq} < 5°$ is much larger than the magnitude of losses for a realistic loss-cone, $\alpha_{LC} \sim 1°$–$2°$. To provide the overestimation factor, we consider the ratio of electrons with $\alpha_{eq} = 5°$ and with $\alpha_{eq} = 1°$–$2°$ from our simulations. In our simulation, we stop integration of electron trajectories at the equatorial crossing if $\alpha_{eq} < 5°$, but the last resonant interaction (before this crossing) may move electrons to smaller

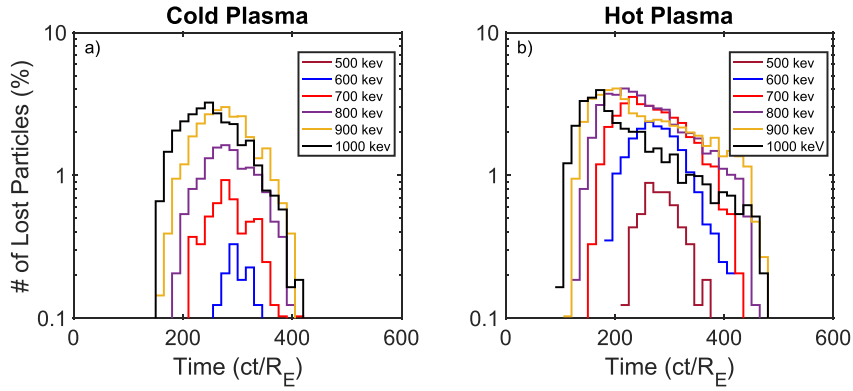

Figure 11. Comparison of the percentage of electrons scattered below $\alpha_{eq} < 5°$ in the system with whistler and EMIC waves for cold (a) and hot (b) plasma dispersion for initial energies ∈ [400, 1,000] keV and the same wave intensities of EMIC and whistler waves as shown in Figures 10e and 10f.

pitch-angles, that is, for $\alpha_{eq} < 5°$, we have the distribution of electron pitch-angles. The ratio of the number of particles within $\alpha_{eq} = 5°$ and with $\alpha_{eq} = 2°$ is about 10, and this ratio reaches 100 for $\alpha_{eq} = 1°$ (see the cumulative distribution of $\alpha_{eq} < 5°$ in Figure S5 of Supporting Information S1). Thus, using a multiplicative factor of 1/10−1/100 to losses shown in Figure 10 should provide a conservative estimate of actual electron losses due to combined resonant interaction with whistler and EMIC waves (note that by stopping numerical integration when $\alpha_{eq} < 5°$ in simulations does not allow wave-particle interactions to flatten the $\alpha_{eq} < 5°$ pitch-angle distribution, i.e., the real multiplicative factor may vary between $1/10 - 1/100$ and ∼1).

Figure 10a shows energies resonating only with whistler waves. Lower energy (∼ 10 keV) electrons are scattered faster, whereas the scattering of ∼ 100 keV electrons requires more time and higher wave amplitudes (these electrons are scatted below 5° only at the middle of time interval when the wave amplitude reaches the maximum value, see bottom panels). Such low losses of ∼ 100 keV electrons are due to phase trapping that is most effective at these energies: the resonant latitude of ∼ 100 keV electrons with small pitch-angles ensures strong wave intensity growth along the electron trajectory, and thus many electrons may experience trapping that move them to high pitch-angles (see, e.g., Artemyev et al., 2021; Vainchtein et al., 2018 for distributions of the trapping probability by field-aligned whistler waves with a peak around ∼ 100 keV and small pitch-angles). Figure 10b shows high energies, some of which may resonate with EMIC waves. Electrons with initial energies $\sim 700 - 1,000$ keV cannot interact resonantly with EMIC waves without an additional acceleration. But these electrons also have a very low probability of trapping (see Artemyev et al., 2021; Vainchtein et al., 2018) and they experience a quick scattering toward small pitch-angles due to phase-bunching. This explains the significant percentage of electron losses and why these losses are mostly observed at the middle of the simulation interval when the wave amplitude reaches sufficiently high values to drive nonlinear resonant scattering (phase bunching). The initial electron ensemble does not include particles with energies above 1 MeV. Thus, all losses of electrons at these energies are due to an acceleration of initially < 1 MeV electrons due to trapping by whistler wave (including turning acceleration) and their subsequent scattering by the EMIC wave (see Figures 8d–8f examples). This explains why > 1 MeV electron losses are observed only at the end of the simulation interval: these electrons first need some time to be trapped (around the middle of the interval when the whistler wave is the most intense) and accelerated, before interacting resonantly with the EMIC wave (at $t \sim (300–400)R/c$) when E_{min} reaches its lowest levels. Decreasing the EMIC wave frequency to $0.5f_{cp}$ does not change the dynamics (losses) of sub-relativistic electrons resonating with whistlers-mode waves (compare Figure 10a and Figure 10c), but significantly decrease scattering of 700–800 keV electrons (compare Figure 10b and Figure 10d), because EMIC waves at lower frequencies do not resonate with such energies and only non-resonant effects (Chen et al., 2016) and whistler phase bunching can contribute to losses at these energies.

To investigate hot plasma effects on the resonant interaction of electrons with EMIC waves, we repeat simulation results from Figures 10a and 10b for [0.4, 1] MeV electrons with the cold dispersion and with an increased k_{EMIC} value due to the hot ion contribution. Figure 11 compares precipitation patterns for these two systems (note we use only electrons with initial energies ∈ [400, 1,000] keV for these runs). All precipitations of < 1 MeV electrons

in the simulation with the cold plasma dispersion are due to the phase bunching by whistler waves around the middle of the simulation interval when the wave amplitude reaches its maximum. In the simulation with the hot plasma effect, we see stronger precipitations of >700 keV electrons that can more easily interact resonantly with the EMIC wave due to the increased k_{EMIC} that corresponds to a decreased E_{min}. Precipitations due to scattering by EMIC waves do not require nonlinear resonant interaction, because even diffusive scattering by the EMIC wave is very strong. The time range with significant electron precipitations is also longer for the simulation with hot plasma effects.

5. Discussion

We examined an interesting event (and quite typical for intervals with strong compressional ULF waves, see Zhang et al., 2020) of simultaneously observed whistler and EMIC waves. These two wave modes are generated by different electron and ion populations (transversely anisotropic electrons are responsible for wave generation, whereas transversely anisotropic ions generate EMIC waves, see Kennel & Petschek, 1966; Sagdeev & Shafranov, 1961). Due to the different drift paths of such anisotropic particle populations injected from the plasma sheet (electrons are drifting dawnwards and ions—duskwards), the MLT range where both wave modes can be generated together is insignificant (Shprits et al., 2006; Thorne, 2010). However, the presence of an external modulation of such ion and electron distributions by ULF compressional waves renders both ion and electron populations unstable at the same place and time generating concurrently both whistler and EMIC waves. Although we examined this mechanism of wave generation at quite large *L*-shells, where ULF waves likely propagate from the magnetopause (Zhang et al., 2020), similar coupling of compressional ULF waves and whistler wave/EMIC waves has been observed at lower *L*-shells (Kitamura et al., 2021; W. Li, Thorne, et al., 2011; Liu et al., 2019; Xia et al., 2016, 2020). Therefore, the combined effects of whistler and EMIC waves may indeed materialize, providing very rapid and spatially localized relativistic electron losses (Mourenas, Artemyev, Ma, et al., 2016; Zhang et al., 2017), that would resemble electron flux dropouts frequently observed in the outer radiation belt (Green et al., 2004; Onsager et al., 2002; Su et al., 2016).

The combined resonant interactions of electrons with whistler and EMIC waves can result in enhanced precipitations of relativistic electrons, even when the initial electron population does not contain such high energies. The nonlinear resonant acceleration (the turning acceleration due to the phase trapping, see Furuya et al., 2008; Omura et al., 2007) of electrons by whistler waves creates a new relativistic population that is then quickly scattered toward the loss-cone by EMIC waves. Even if the EMIC wave amplitude is insufficiently large to support the nonlinear resonances, quasi-linear scattering rates are sufficiently high to provide such losses (Kersten et al., 2014; Ni et al., 2015). Because theoretically (Grach et al., 2021; Kubota & Omura, 2017) and observationally (Blum et al., 2015; Capannolo, Li, Ma, Chen, et al., 2019; Douma et al., 2018; Yahnin et al., 2017) EMIC waves are associated with relativistic electron micro-bursts, very transient and intense precipitations, EMIC waves are often considered as a driver of relativistic electron flux depletion in the radiation belt (Drozdov et al., 2017; Ma et al., 2015; Shprits et al., 2016). Results presented in our study show that EMIC waves may precipitate locally accelerated electrons, and thus can generate relativistic micro-bursts even in the initial absence of significant fluxes of relativistic electrons.

Although electron resonances with EMIC waves are generally associated with losses of relativistic electrons (Bashir & Ilie, 2018; Miyoshi et al., 2008; Rodger et al., 2015; Usanova et al., 2014; Zhang, Li, Ma, et al., 2016), there are appears to be evidence of simultaneous precipitations at lower energies (Capannolo et al., 2018; Hendry et al., 2017). Such precipitations below the minimum resonant energy (determined from the cold plasma dispersion of EMIC waves, see Summers & Thorne, 2003) may be explained by non-resonant electron scattering by EMIC waves (Chen et al., 2016), whereas the hot plasma (ion) effect on EMIC dispersion is believed to increase this minimum energy (Cao et al., 2017; Chen et al., 2019). Our analysis of EMIC wave generation and dispersion for the observed ion distribution functions confirms the increase of the minimum resonant energy for the most intense EMIC waves (with maximum growth rates). However, for the higher-frequency part of the observed EMIC spectrum, hot plasma effects can decrease the minimum resonant energy. This may potentially explain some precipitations of non-relativistic electrons, but a more detailed parametric investigation would be required to determine the variability range of the minimum resonant energy for observed EMIC and ion characteristics.

6. Conclusions

The main conclusions of our investigation of electron resonant interactions with ULF-modulated EMIC and whistler waves are as follows:

1. The compressive ULF modulation of electron populations is sufficiently strong to drive the generation of intense whistler waves interacting with resonant electrons in the nonlinear regime, requiring the inclusion of phase trapping and bunching effects. Such intense nonlinear interactions allow whistler waves to scatter (due to phase bunching) ≤ 100 keV electrons and accelerate $\sim 300-500$ keV electrons up to relativistic energies very effectively, within a half of the ULF period. Therefore, the nonlinear resonance effects should be taken into account in investigations of energetic electron dynamics for events with ULF-modulated whistler waves.
2. The combined effects of electron nonlinear interaction with whistler waves (phase trapping acceleration) and diffusive scattering by EMIC waves can result in precipitation of relativistic electrons even in the absence of significant fluxes of electrons at such high energies at the initial distribution. Therefore, observations (e.g., low-altitude and ground-based) of relativistic electron precipitation should not be always interpreted as losses of initial background electron fluxes.
3. The hot plasma (ion) effects significantly increase the minimum energy of electrons resonating with the most intense EMIC waves, but can decrease this minimum energy for the higher-frequency part of EMIC spectra corresponding to smaller wave intensity (marginally stable waves). Therefore, a proper evaluation of the lowest energy for electron resonant scattering by EMIC waves with the hot plasma dispersion requires consideration of the entire unstable wave frequency range.

Data Availability Statement

The authors would like to thank the THEMIS instrument teams for excellent data that have been downloaded from http://themis.ssl.berkeley.edu, respectively. Data analysis was done using SPEDAS V3.1, see Angelopoulos et al. (2019).

Acknowledgments
We are grateful to Dr. D. Mourenas for his useful comments and suggestions on this study. Work of Muhammad Fraz Bashir, Anton Artemyev, and Xiaojia Zhang are supported by NSF grant #2021749 and NASA grants #80NSSC20K1270 and #80NSSC20K1578. Muhammad Fraz Bashir and Vassilis Angelopoulos acknowledge the support through NASA contract NAS5-02099 for use of data from the THEMIS.

References

Agapitov, O. V., Artemyev, A., Krasnoselskikh, V., Khotyaintsev, Y. V., Mourenas, D., Breuillard, H., & Rolland, G. (2013). Statistics of whistler mode waves in the outer radiation belt: Cluster STAFF-SA measurements. *Journal of Geophysical Research*, *118*, 3407–3420. https://doi.org/10.1002/jgra.50312

Agapitov, O. V., Artemyev, A. V., Mourenas, D., Mozer, F. S., & Krasnoselskikh, V. (2015). Empirical model of lower band chorus wave distribution in the outer radiation belt. *Journal of Geophysical Research: Space Physics*, *120*(12), 10,425–10,442. https://doi.org/10.1002/2015ja021829

Agapitov, O. V., Mourenas, D., Artemyev, A. V., Mozer, F. S., Hospodarsky, G., Bonnell, J., & Krasnoselskikh, V. (2018). Synthetic empirical chorus wave model from combined Van Allen Probes and cluster statistics. *Journal of Geophysical Research: Space Physics*, *123*(1), 297–314. https://doi.org/10.1002/2017ja024843

Albert, J. M. (2000). Gyroresonant interactions of radiation belt particles with a monochromatic electromagnetic wave. *Journal of Geophysical Research: Space Physics*, *105*(A9), 21191–21209. https://doi.org/10.1029/2000ja000008

Albert, J. M. (2001). Comparison of pitch angle diffusion by turbulent and monochromatic whistler waves. *Journal of Geophysical Research: Space Physics*, *106*(A5), 8477–8482. https://doi.org/10.1029/2000ja000304

Albert, J. M. (2002). Nonlinear interaction of outer zone electrons with VLF waves. *Geophysical Research Letters*, *29*(8), 116–1. https://doi.org/10.1029/2001gl013941

Albert, J. M. (2010). Diffusion by one wave and by many waves. *Journal of Geophysical Research: Space Physics*, *115*(A3), A00F05. https://doi.org/10.1029/2009ja014732

Albert, J. M., & Bortnik, J. (2009). Nonlinear interaction of radiation belt electrons with electromagnetic ion cyclotron waves. *Geophysical Research Letters*, *36*, 12110. https://doi.org/10.1029/2009GL038904

Albert, J. M., Tao, X., & Bortnik, J. (2013). Aspects of nonlinear wave-particle interactions. In D. Summers, I. U. Mann, D. N. Baker, & M. Schulz (Eds.), *Dynamics of the Earth's radiation belts and inner magnetosphere* (pp. 255–264). American Geophysical Union. https://doi.org/10.1029/2012GM001324

Allanson, O., Watt, C. E. J., Allison, H. J., & Ratcliffe, H. (2021). Electron diffusion and advection during nonlinear interactions with whistler mode waves. *Journal of Geophysical Research: Space Physics*, *126*(5), e28793. https://doi.org/10.1029/2020JA028793

Allanson, O., Watt, C. E. J., Ratcliffe, H., Allison, H. J., Meredith, N. P., Bentley, S. N., & Glauert, S. A. (2020). Particle-in-cell experiments examine electron diffusion by whistler-mode waves: 2. Quasi-linear and nonlinear dynamics. *Journal of Geophysical Research: Space Physics*, *125*(7), e27949. https://doi.org/10.1029/2020JA027949

Allison, H. J., & Shprits, Y. Y. (2020). Local heating of radiation belt electrons to ultra-relativistic energies. *Nature Communications*, *11*, 4533. https://doi.org/10.1038/s41467-020-18053-z

Andronov, A. A., & Trakhtengerts, V. Y. (1964). Kinetic instability of the Earth's outer radiation belt. *Geomagnetism and Aeronomy*, *4*, 233–242.

Angelopoulos, V. (2008). The THEMIS mission. *Space Science Reviews*, *141*, 5–34. https://doi.org/10.1007/s11214-008-9336-1

Angelopoulos, V., Cruce, P., Drozdov, A., Grimes, E. W., Hatzigeorgiu, N., King, D. A., & Schroeder, P. (2019). The space physics environment data analysis system (SPEDAS). *Space Science Reviews*, *215*, 9. https://doi.org/10.1007/s11214-018-0576-4

Angelopoulos, V., Sibeck, D., Carlson, C. W., McFadden, J. P., Larson, D., Lin, R. P., et al. (2008). First results from the THEMIS mission. *Space Science Reviews*, *141*(1–4), 453–476. https://doi.org/10.1007/s11214-008-9378-4

Artemyev, A. V., Neishtadt, A. I., Vainchtein, D. L., Vasiliev, A. A., Vasko, I. Y., & Zelenyi, L. M. (2018). Trapping (capture) into resonance and scattering on resonance: Summary of results for space plasma systems. *Communications in Nonlinear Science and Numerical Simulations*, *65*, 111–160. https://doi.org/10.1016/j.cnsns.2018.05.004

Artemyev, A. V., Neishtadt, A. I., Vasiliev, A. A., & Mourenas, D. (2016). Kinetic equation for nonlinear resonant wave-particle interaction. *Physics of Plasmas*, *23*(9), 090701. https://doi.org/10.1063/1.4962526

Artemyev, A. V., Neishtadt, A. I., Vasiliev, A. A., Zhang, X.-J., Mourenas, D., & Vainchtein, D. (2021). Long-term dynamics driven by resonant wave-particle interactions: From Hamiltonian resonance theory to phase space mapping. *Journal of Plasma Physics*, *87*(2), 835870201. https://doi.org/10.1017/S0022377821000246

Artemyev, A. V., Vasiliev, A. A., Mourenas, D., Agapitov, O. V., & Krasnoselskikh, V. V. (2014). Electron scattering and nonlinear trapping by oblique whistler waves: The critical wave intensity for nonlinear effects. *Physics of Plasmas*, *21*(10), 102903. https://doi.org/10.1063/1.4897945

Artemyev, A. V., Vasiliev, A. A., Mourenas, D., Neishtadt, A. I., Agapitov, O. V., & Krasnoselskikh, V. (2015). Probability of relativistic electron trapping by parallel and oblique whistler-mode waves in Earth's radiation belts. *Physics of Plasmas*, *22*(11), 112903. https://doi.org/10.1063/1.4935842

Auster, H. U., Glassmeier, K. H., Magnes, W., Aydogar, O., Baumjohann, W., Constantinescu, D., & Wiedemann, M. (2008). The THEMIS fluxgate magnetometer. *Space Science Reviews*, *141*, 235–264. https://doi.org/10.1007/s11214-008-9365-9

Bashir, M. F., & Ilie, R. (2018). A New N + Band of Electromagnetic Ion Cyclotron Waves in Multi-Ion Cold Plasmas. *Geophysical Research Letters 45*(19), 10,150–10,159. https://doi.org/10.1029/2018gl080280

Bell, T. F. (1984). The nonlinear gyroresonance interaction between energetic electrons and coherent VLF waves propagating at an arbitrary angle with respect to the earth's magnetic field. *Journal of Geophysical Research*, *89*(A2), 905. https://doi.org/10.1029/ja089ia02p00905

Blum, L. W., Agapitov, O., Bonnell, J. W., Kletzing, C., & Wygant, J. (2016). EMIC wave spatial and coherence scales as determined from multi-point Van Allen Probe measurements. *Geophysical Research Letters*, *43*, 4799–4807. https://doi.org/10.1002/2016GL068799

Blum, L. W., Bonnell, J. W., Agapitov, O., Paulson, K., & Kletzing, C. (2017). EMIC wave scale size in the inner magnetosphere: Observations from the dual Van Allen Probes. *Geophysical Research Letters*, *44*, 1227–1233. https://doi.org/10.1002/2016GL072316

Blum, L. W., Halford, A., Millan, R., Bonnell, J. W., Goldstein, J., Usanova, M., & Li, X. (2015). Observations of coincident EMIC wave activity and duskside energetic electron precipitation on 18-19 January 2013. *Geophysical Research Letters*, *42*, 5727–5735. https://doi.org/10.1002/2015GL065245

Blum, L. W., MacDonald, E. A., Gary, S. P., Thomsen, M. F., & Spence, H. E. (2009). Ion observations from geosynchronous orbit as a proxy for ion cyclotron wave growth during storm times. *Journal of Geophysical Research: Space Physics*, *114*(A10), A10214. https://doi.org/10.1029/2009JA014396

Bonnell, J. W., Mozer, F. S., Delory, G. T., Hull, A. J., Ergun, R. E., Cully, C. M., & Harvey, P. R. (2008). The electric field instrument (EFI) for THEMIS. *Space Science Reviews*, *141*, 303–341. https://doi.org/10.1007/s11214-008-9469-2

Bortnik, J., Thorne, R. M., & Inan, U. S. (2008). Nonlinear interaction of energetic electrons with large amplitude chorus. *Geophysical Research Letters*, *35*, 21102. https://doi.org/10.1029/2008GL035500

Cao, J., Shprits, Y. Y., Ni, B., & Zhelavskaya, I. S. (2017). Scattering of ultra-relativistic electrons in the Van Allen radiation belts accounting for hot plasma effects. *Scientific Reports*, *7*, 17719. https://doi.org/10.1038/s41598-017-17739-7

Capannolo, L., Li, W., Ma, Q., Chen, L., Shen, X. C., Spence, H. E., & Redmon, R. J. (2019). Direct observation of sub-relativistic electron precipitation potentially driven by EMIC waves. *Geophysical Research Letters*. https://doi.org/10.1029/2019GL084202

Capannolo, L., Li, W., Ma, Q., Shen, X. C., Zhang, X. J., Redmon, R. J., & Raita, T. (2019). Energetic electron precipitation: Multievent analysis of its spatial extent during EMIC wave activity. *Journal of Geophysical Research: Space Physics*, *124*(4), 2466–2483. https://doi.org/10.1029/2018JA026291

Capannolo, L., Li, W., Ma, Q., Zhang, X.-J., Redmon, R. J., Rodriguez, J. V., & Reeves, G. D. (2018). Understanding the driver of energetic electron precipitation using coordinated multisatellite measurements. *Geophysical Research Letters*, *45*, 6755–6765. https://doi.org/10.1029/2018GL078604

Cattell, C., Wygant, J. R., Goetz, K., Kersten, K., Kellogg, P. J., von Rosenvinge, T., et al. (2008). Discovery of very large amplitude whistler-mode waves in Earth's radiation belts. *Geophysical Research Letters*, *35*(1), L01105. https://doi.org/10.1029/2007gl032009

Chen, L., Thorne, R. M., & Bortnik, J. (2011). The controlling effect of ion temperature on EMIC wave excitation and scattering. *Geophysical Research Letters*, *38*(16), L16109. https://doi.org/10.1029/2011GL048653

Chen, L., Thorne, R. M., Bortnik, J., & Zhang, X.-J. (2016). Nonresonant interactions of electromagnetic ion cyclotron waves with relativistic electrons. *Journal of Geophysical Research: Space Physics*, *121*(10), 9913–9925. https://doi.org/10.1002/2016ja022813

Chen, L., Zhu, H., & Zhang, X. (2019). Wavenumber analysis of EMIC waves. *Geophysical Research Letters*, *46*(11), 5689–5697. https://doi.org/10.1029/2019GL082686

Cully, C. M., Ergun, R. E., Stevens, K., Nammari, A., & Westfall, J. (2008). The THEMIS digital fields board. *Space Science Reviews*, *141*, 343–355. https://doi.org/10.1007/s11214-008-9417-1

Demekhov, A. G., Trakhtengerts, V. Y., Rycroft, M. J., & Nunn, D. (2006). Electron acceleration in the magnetosphere by whistler-mode waves of varying frequency. *Geomagnetism and Aeronomy*, *46*, 711–716. https://doi.org/10.1134/S0016793206060053

Denton, R. E., Jordanova, V. K., & Bortnik, J. (2015). Resonance of relativistic electrons with electromagnetic ion cyclotron waves. *Geophysical Research Letters*, *42*, 8263–8270. https://doi.org/10.1002/2015GL064379

Douma, E., Rodger, C. J., Clilverd, M. A., Hendry, A. T., Engebretson, M. J., & Lessard, M. R. (2018). Comparison of relativistic microburst activity seen by SAMPEX with ground-based wave measurements at Halley, Antarctica. *Journal of Geophysical Research: Space Physics*, *123*(2), 1279–1294. https://doi.org/10.1002/2017JA024754

Drozdov, A. Y., Shprits, Y. Y., Orlova, K. G., Kellerman, A. C., Subbotin, D. A., Baker, D. N., et al. (2015). Energetic, relativistic, and ultrarelativistic electrons: Comparison of long-term VERB code simulations with Van Allen Probes measurements. *Journal of Geophysical Research: Space Physics*, *120*(5), 3574–3587. https://doi.org/10.1002/2014ja020637

Drozdov, A. Y., Shprits, Y. Y., Usanova, M. E., Aseev, N. A., Kellerman, A. C., & Zhu, H. (2017). EMIC wave parameterization in the long-term VERB code simulation. *Journal of Geophysical Research: Space Physics*, *122*(8), 8488–8501. https://doi.org/10.1002/2017ja024389

Fried, B. D., & Conte, S. D. (1961). *The plasma dispersion function*. Academic Press.

Furuya, N., Omura, Y., & Summers, D. (2008). Relativistic turning acceleration of radiation belt electrons by whistler mode chorus. *Journal of Geophysical Research: Space Physics*, *113*(A4), A04224. https://doi.org/10.1029/2007ja012478

Gail, W. B., & Inan, U. S. (1990). Characteristics of wave-particle interactions during sudden commencements: 2. Spacecraft observations. *Journal of Geophysical Research: Space Physics*, *95*(A1), 139. https://doi.org/10.1029/ja095ia01p00139

Glauert, S. A., & Horne, R. B. (2005). Calculation of pitch angle and energy diffusion coefficients with the PADIE code. *Journal of Geophysical Research: Space Physics*, *110*(A4), A04206. https://doi.org/10.1029/2004ja010851

Grach, V. S., & Demekhov, A. G. (2018). Resonant interaction of relativistic electrons with electromagnetic ion-cyclotron waves. II. Integral parameters of interaction regimes. *Radiophysics and Quantum Electronics*, *61*(6), 389–401. https://doi.org/10.1007/s11141-018-9900-9

Grach, V. S., & Demekhov, A. G. (2020). Precipitation of relativistic electrons under resonant interaction with electromagnetic ion cyclotron wave packets. *Journal of Geophysical Research: Space Physics*, *125*(2), e27358. https://doi.org/10.1029/2019JA027358

Grach, V. S., Demekhov, A. G., & Larchenko, A. V. (2021). Resonant interaction of relativistic electrons with realistic electromagnetic ion-cyclotron wave packets. *Earth Planets and Space*, *73*(1), 129. https://doi.org/10.1186/s40623-021-01453-w

Green, J. C., Onsager, T. G., O'Brien, T. P., & Baker, D. N. (2004). Testing loss mechanisms capable of rapidly depleting relativistic electron flux in the Earth's outer radiation belt. *Journal of Geophysical Research: Space Physics*, *109*(A12), A12211. https://doi.org/10.1029/2004ja010579

Hendry, A. T., Rodger, C. J., & Clilverd, M. A. (2017). Evidence of sub-MeV EMIC-driven electron precipitation. *Geophysical Research Letters*, *44*, 1210–1218. https://doi.org/10.1002/2016GL071807

Horne, R. B., Kersten, T., Glauert, S. A., Meredith, N. P., Boscher, D., Sicard-Piet, A., & Li, W. (2013). A new diffusion matrix for whistler mode chorus waves. *Journal of Geophysical Research*, *118*, 6302–6318. https://doi.org/10.1002/jgra.50594

Horne, R. B., Thorne, R. M., Shprits, Y. Y., Meredith, N. P., Glauert, S. A., Smith, A. J., & Decreau, P. M. E. (2005). Wave acceleration of electrons in the Van Allen radiation belts. *Nature*, *437*, 227–230. https://doi.org/10.1038/nature03939

Hsieh, Y.-K., Kubota, Y., & Omura, Y. (2020). Nonlinear evolution of radiation belt electron fluxes interacting with oblique whistler mode chorus emissions. *Journal of Geophysical Research: Space Physics*, *125*, e2019JA027465. https://doi.org/10.1029/2019JA027465

Hsieh, Y.-K., & Omura, Y. (2017a). Nonlinear dynamics of electrons interacting with oblique whistler mode chorus in the magnetosphere. *Journal of Geophysical Research*, *122*, 675–694. https://doi.org/10.1002/2016JA023255

Hsieh, Y.-K., & Omura, Y. (2017b). Study of wave-particle interactions for whistler mode waves at oblique angles by utilizing the gyroaveraging method. *Radio Science*, *52*(10), 1268–1281. https://doi.org/10.1002/2017rs006245

Hsieh, Y.-K., Omura, Y., & Kubota, Y. (2021). Energetic electron precipitation induced by oblique whistler mode chorus emissions. *Journal of Geophysical Research: Space Physics*, e2021JA029583. https://doi.org/10.1029/2021ja029583

Jun, C. W., Yue, C., Bortnik, J., Lyons, L. R., Nishimura, Y., & Kletzing, C. (2019). EMIC wave properties associated with and without injections in the inner magnetosphere. *Journal of Geophysical Research: Space Physics*, *124*(3), 2029–2045. https://doi.org/10.1029/2018JA026279

Karpman, V. I. (1974). Nonlinear effects in the ELF waves propagating along the magnetic field in the magnetosphere. *Space Science Reviews*, *16*(3), 361–388. https://doi.org/10.1007/bf00171564

Kasahara, S., Miyoshi, Y., Yokota, S., Kasahara, Y., Matsuda, S., Kumamoto, A., & Shinohara, I. (2018). Pulsating aurora from electron scattering by chorus waves. *Nature*, *554*, 337–340. https://doi.org/10.1038/nature25505

Kennel, C. F., & Engelmann, F. (1966). Velocity space diffusion from weak plasma turbulence in a magnetic field. *Physics of Fluids*, *9*(12), 2377. https://doi.org/10.1063/1.1761629

Kennel, C. F., & Petschek, H. E. (1966). Limit on stably trapped particle fluxes. *Journal of Geophysical Research*, *71*, 1–28.

Kersten, T., Horne, R. B., Glauert, S. A., Meredith, N. P., Fraser, B. J., & Grew, R. S. (2014). Electron losses from the radiation belts caused by EMIC waves. *Journal of Geophysical Research: Space Physics*, *119*(11), 8820–8837. https://doi.org/10.1002/2014ja020366

Kitamura, N., Shoji, M., Nakamura, S., Kitahara, M., Amano, T., Omura, Y., & Burch, J. L. (2021). Energy transfer between hot protons and electromagnetic ion cyclotron waves in compressional Pc5 ultra low frequency waves. *Journal of Geophysical Research: Space Physics*, *126*(5), e28912. https://doi.org/10.1029/2020JA028912

Kubota, Y., & Omura, Y. (2017). Rapid precipitation of radiation belt electrons induced by EMIC rising tone emissions localized in longitude inside and outside the plasmapause. *Journal of Geophysical Research: Space Physics*, *122*(1), 293–309. https://doi.org/10.1002/2016JA023267

Kubota, Y., Omura, Y., & Summers, D. (2015). Relativistic electron precipitation induced by EMIC-triggered emissions in a dipole magnetosphere. *Journal of Geophysical Research: Space Physics*, *120*(6), 4384–4399. https://doi.org/10.1002/2015JA021017

Le Contel, O., Roux, A., Robert, P., Coillot, C., Bouabdellah, A., de La Porte, B., et al. (2008). First results of the THEMIS search coil magnetometers. *Space Science Reviews*, *141*(1–4), 509–534. https://doi.org/10.1007/s11214-008-9371-y

Li, W., Bortnik, J., Thorne, R. M., & Angelopoulos, V. (2011). Global distribution of wave amplitudes and wave normal angles of chorus waves using THEMIS wave observations. *Journal of Geophysical Research: Space Physics*, *116*(A12), A12205. https://doi.org/10.1029/2011ja017035

Li, W., & Hudson, M. K. (2019). Earth's Van Allen radiation belts: From discovery to the Van Allen probes era. *Journal of Geophysical Research: Space Physics*, *124*(11), 8319–8351. https://doi.org/10.1029/2018JA025940

Li, W., Thorne, R. M., Bortnik, J., Nishimura, Y., & Angelopoulos, V. (2011). Modulation of whistler mode chorus waves: 1. Role of compressional Pc4-5 pulsations. *Journal of Geophysical Research: Space Physics*, *116*(A6), A06205. https://doi.org/10.1029/2010ja016312

Li, W., Thorne, R. M., Ma, Q., Ni, B., Bortnik, J., Baker, D. N., et al. (2014). Radiation belt electron acceleration by chorus waves during the 17 March 2013 storm. *Journal of Geophysical Research: Space Physics*, *119*(6), 4681–4693. https://doi.org/10.1002/2014ja019945

Li, Z., Millan, R. M., Hudson, M. K., Woodger, L. A., Smith, D. M., Chen, Y., & Spence, H. E. (2014). Investigation of EMIC wave scattering as the cause for the BARREL 17 January 2013 relativistic electron precipitation event: A quantitative comparison of simulation with observations. *Geophysical Research Letters*, *41*(24), 8722–8729. https://doi.org/10.1002/2014GL062273

Liu, N., Su, Z., Gao, Z., Zheng, H., Wang, Y., & Wang, S. (2019). Magnetospheric chorus, exohiss, and magnetosonic emissions simultaneously modulated by fundamental toroidal standing Alfvén waves following solar wind dynamic pressure fluctuations. *Geophysical Research Letters*, *46*(4), 1900–1910. https://doi.org/10.1029/2018GL081500

Lyons, L. R., & Williams, D. J. (Eds.). (1984). *Quantitative aspects of magnetospheric physics*. Reidel Publishing Company.

Ma, Q., Artemyev, A. V., Mourenas, D., Li, W., Thorne, R. M., Kletzing, C. A., et al. (2017). Very oblique whistler mode propagation in the radiation belts: Effects of hot plasma and Landau damping. *Geophysical Research Letters*, *44*(24), 12057–12066. https://doi.org/10.1002/2017GL075892

Ma, Q., Li, W., Bortnik, J., Thorne, R. M., Chu, X., Ozeke, L. G., & Claudepierre, S. G. (2018). Quantitative evaluation of radial diffusion and local acceleration processes during GEM challenge events. *Journal of Geophysical Research: Space Physics*, *123*(3), 1938–1952. https://doi.org/10.1002/2017JA025114

Ma, Q., Li, W., Thorne, R. M., Ni, B., Kletzing, C. A., Kurth, W. S., & Angelopoulos, V. (2015). Modeling inward diffusion and slow decay of energetic electrons in the Earth's outer radiation belt. *Geophysical Research Letters*, *42*, 987–995. https://doi.org/10.1002/2014GL062977

McFadden, J. P., Carlson, C. W., Larson, D., Ludlam, M., Abiad, R., Elliott, B., & Angelopoulos, V. (2008). The THEMIS ESA plasma instrument and in-flight calibration. *Space Science Reviews*, *141*, 277–302. https://doi.org/10.1007/s11214-008-9440-2

Meredith, N. P., Horne, R. B., & Anderson, R. R. (2001). Substorm dependence of chorus amplitudes: Implications for the acceleration of electrons to relativistic energies. *Journal of Geophysical Research: Space Physics*, *106*(A7), 13165–13178. https://doi.org/10.1029/2000ja900156

Meredith, N. P., Horne, R. B., Sicard-Piet, A., Boscher, D., Yearby, K. H., Li, W., & Thorne, R. M. (2012). Global model of lower band and upper band chorus from multiple satellite observations. *Journal of Geophysical Research: Space Physics*, *117*(A10), A10225. https://doi.org/10.1029/2012ja017978

Meredith, N. P., Horne, R. B., Thorne, R. M., & Anderson, R. R. (2003). Favored regions for chorus-driven electron acceleration to relativistic energies in the Earth's outer radiation belt. *Geophysical Research Letters*, *30*(16). https://doi.org/10.1029/2003GL017698

Millan, R. M., & Baker, D. N. (2012). Acceleration of particles to high energies in earth's radiation belts. *Space Science Reviews*, *173*(1–4), 103–131. https://doi.org/10.1007/s11214-012-9941-x

Millan, R. M., & Thorne, R. M. (2007). Review of radiation belt relativistic electron losses. *Journal of Atmospheric and Solar-Terrestrial Physics*, *69*(3), 362–377. https://doi.org/10.1016/j.jastp.2006.06.019

Min, K., Kim, J., Ma, Q., Jun, C.-W., & Liu, K. (2022). Unusual high frequency EMIC waves: Detailed analysis of EMIC wave excitation and energy coupling between EMIC and magnetosonic waves. *Advances in Space Research*, *69*(1), 35–47. https://doi.org/10.1016/j.asr.2021.07.039

Miyoshi, Y., Sakaguchi, K., Shiokawa, K., Evans, D., Albert, J., Connors, M., & Jordanova, V. (2008). Precipitation of radiation belt electrons by EMIC waves, observed from ground and space. *Geophysical Research Letters*, *35*(23), L23101. https://doi.org/10.1029/2008GL035727

Mourenas, D., Artemyev, A. V., Agapitov, O. V., & Krasnoselskikh, V. (2014). Consequences of geomagnetic activity on energization and loss of radiation belt electrons by oblique chorus waves. *Journal of Geophysical Research: Space Physics*, *119*(4), 2775–2796. https://doi.org/10.1002/2013ja019674

Mourenas, D., Artemyev, A. V., Agapitov, O. V., Krasnoselskikh, V., & Li, W. (2014). Approximate analytical solutions for the trapped electron distribution due to quasi-linear diffusion by whistler mode waves. *Journal of Geophysical Research*, *119*, 9962–9977. https://doi.org/10.1002/2014JA020443

Mourenas, D., Artemyev, A. V., Agapitov, O. V., Mozer, F. S., & Krasnoselskikh, V. V. (2016). Equatorial electron loss by double resonance with oblique and parallel intense chorus waves. *Journal of Geophysical Research: Space Physics*, *121*(5), 4498–4517. https://doi.org/10.1002/2015ja022223

Mourenas, D., Artemyev, A. V., Ma, Q., Agapitov, O. V., & Li, W. (2016). Fast dropouts of multi-MeV electrons due to combined effects of EMIC and whistler mode waves. *Geophysical Research Letters*, *43*(9), 4155–4163. https://doi.org/10.1002/2016GL068921

Ni, B., Cao, X., Zou, Z., Zhou, C., Gu, X., Bortnik, J., & Xie, L. (2015). Resonant scattering of outer zone relativistic electrons by multiband EMIC waves and resultant electron loss time scales. *Journal of Geophysical Research*, *120*, 7357–7373. https://doi.org/10.1002/2015JA021466

Nishimura, Y., Bortnik, J., Li, W., Thorne, R. M., Chen, L., Lyons, L. R., & Auster, U. (2011). Multievent study of the correlation between pulsating aurora and whistler mode chorus emissions. *Journal of Geophysical Research: Space Physics*, *116*(A11), A11221. https://doi.org/10.1029/2011JA016876

Nishimura, Y., Bortnik, J., Li, W., Thorne, R. M., Ni, B., Lyons, L. R., & Auster, U. (2013). Structures of dayside whistler-mode waves deduced from conjugate diffuse aurora. *Journal of Geophysical Research: Space Physics*, *118*(2), 664–673. https://doi.org/10.1029/2012JA018242

Omura, Y., Furuya, N., & Summers, D. (2007). Relativistic turning acceleration of resonant electrons by coherent whistler mode waves in a dipole magnetic field. *Journal of Geophysical Research: Space Physics*, *112*(A6), A06236. https://doi.org/10.1029/2006ja012243

Omura, Y., Miyashita, Y., Yoshikawa, M., Summers, D., Hikishima, M., Ebihara, Y., & Kubota, Y. (2015). Formation process of relativistic electron flux through interaction with chorus emissions in the Earth's inner magnetosphere. *Journal of Geophysical Research*, *120*, 9545–9562. https://doi.org/10.1002/2015JA021563

Onsager, T. G., Rostoker, G., Kim, H.-J., Reeves, G. D., Obara, T., Singer, H. J., & Smithtro, C. (2002). Radiation belt electron flux dropouts: Local time, radial, and particle-energy dependence. *Journal of Geophysical Research: Space Physics*, *107*(A11), 1382. https://doi.org/10.1029/2001ja000187

Remya, B., Tsurutani, B. T., Reddy, R. V., Lakhina, G. S., & Hajra, R. (2015). Electromagnetic cyclotron waves in the dayside subsolar outer magnetosphere generated by enhanced solar wind pressure: EMIC wave coherency. *Journal of Geophysical Research: Space Physics*, *120*(9), 7536–7551. https://doi.org/10.1002/2015JA021327

Rodger, C. J., Hendry, A. T., Clilverd, M. A., Kletzing, C. A., Brundell, J. B., & Reeves, G. D. (2015). High-resolution in situ observations of electron precipitation-causing EMIC waves. *Geophysical Research Letters*, *42*(22), 9633–9641. https://doi.org/10.1002/2015GL066581

Runov, A., Angelopoulos, V., Gabrielse, C., Liu, J., Turner, D. L., & Zhou, X.-Z. (2015). Average thermodynamic and spectral properties of plasma in and around dipolarizing flux bundles. *Journal of Geophysical Research*, *120*, 4369–4383. https://doi.org/10.1002/2015JA021166

Sagdeev, R. Z., & Shafranov, V. D. (1961). On the instability of a plasma with an anisotropic distribution of velocities in a magnetic field. *Soviet Physics JETP*, *12*(1), 130–132. http://www.jetp.ras.ru/cgi-bin/dn/e_012_01_0130.pdf

Sazhin, S. (1993). *Whistler-mode waves in a hot plasma*. Cambridge University Press. https://doi.org/10.1017/CBO9780511525094

Schulz, M., & Lanzerotti, L. J. (1974). *Particle diffusion in the radiation belts*. Springer.

Shapiro, V. D., & Sagdeev, R. Z. (1997). Nonlinear wave-particle interaction and conditions for the applicability of quasilinear theory. *Physics Reports*, *283*(1–4), 49–71. https://doi.org/10.1016/S0370-1573(96)00053-1

Shklyar, D. R. (1981). Stochastic motion of relativistic particles in the field of a monochromatic wave. *Soviet Physics Journal of Experimental and Theoretical Physics*, *53*, 1197–1192. https://ui.adsabs.harvard.edu/abs/1981ZhETF..80.2272S/abstract

Shklyar, D. R. (2011). On the nature of particle energization via resonant wave-particle interaction in the inhomogeneous magnetospheric plasma. *Annales Geophysicae*, *29*, 1179–1188. https://doi.org/10.5194/angeo-29-1179-2011

Shklyar, D, & Matsumoto, H. (2009). Oblique whistler-mode waves in the inhomogeneous magnetospheric plasma: Resonant interactions with energetic charged particles. *Surveys in Geophysics*, *30*(2), 55–104. https://doi.org/10.1007/s10712-009-9061-7

Shprits, Y. Y., Chen, L., & Thorne, R. M. (2009). Simulations of pitch-angle scattering of relativistic electrons with MLT-dependent diffusion coefficients. *Journal of Geophysical Research: Space Physics*, *114*(A3), A03219. https://doi.org/10.1029/2008ja013695

Shprits, Y. Y., Drozdov, A. Y., Spasojevic, M., Kellerman, A. C., Usanova, M. E., Engebretson, M. J., & Aseev, N. A. (2016). Wave-induced loss of ultra-relativistic electrons in the Van Allen radiation belts. *Nature Communications*, *7*, 12883. https://doi.org/10.1038/ncomms12883

Shprits, Y. Y., Kellerman, A., Aseev, N., Drozdov, A. Y., & Michaelis, I. (2017). Multi-MeV electron loss in the heart of the radiation belts. *Geophysical Research Letters*, *44*(3), 1204–1209. https://doi.org/10.1002/2016GL072258

Shprits, Y. Y., Thorne, R. M., Horne, R. B., & Summers, D. (2006). Bounce-averaged diffusion coefficients for field-aligned chorus waves. *Journal of Geophysical Research*, *111*, 10225. https://doi.org/10.1029/2006JA011725

Silin, I., Mann, I. R., Sydora, R. D., Summers, D., & Mace, R. L. (2011). Warm plasma effects on electromagnetic ion cyclotron wave MeV electron interactions in the magnetosphere. *Journal of Geophysical Research: Space Physics*, *116*(A5), A05215. https://doi.org/10.1029/2010JA016398

Stix, T. H. (1962). *The theory of plasma waves*. McGraw-Hill.

Su, Z., Gao, Z., Zhu, H., Li, W., Zheng, H., Wang, Y., et al. (2016). Nonstorm time dropout of radiation belt electron fluxes on 24 September 2013. *Journal of Geophysical Research: Space Physics*, *121*(7), 6400–6416. https://doi.org/10.1002/2016ja022546

Summers, D., & Omura, Y. (2007). Ultra-relativistic acceleration of electrons in planetary magnetospheres. *Geophysical Research Letters*, *34*, 24205. https://doi.org/10.1029/2007GL032226

Summers, D., & Thorne, R. M. (2003). Relativistic electron pitch-angle scattering by electromagnetic ion cyclotron waves during geomagnetic storms. *Journal of Geophysical Research: Space Physics*, *108*(A4), 1143. https://doi.org/10.1029/2002ja009489

Tao, X., Bortnik, J., Albert, J. M., Liu, K., & Thorne, R. M. (2011). Comparison of quasilinear diffusion coefficients for parallel propagating whistler mode waves with test particle simulations. *Geophysical Research Letters*, *38*(6), L06105. https://doi.org/10.1029/2011gl046787

Tao, X., Bortnik, J., Albert, J. M., & Thorne, R. M. (2012). Comparison of bounce-averaged quasi-linear diffusion coefficients for parallel propagating whistler mode waves with test particle simulations. *Journal of Geophysical Research: Space Physics*, *117*(A10), A10205. https://doi.org/10.1029/2012ja017931

Tao, X., Thorne, R. M., Li, W., Ni, B., Meredith, N. P., & Horne, R. B. (2011). Evolution of electron pitch angle distributions following injection from the plasma sheet. *Journal of Geophysical Research: Space Physics*, *116*(A4), A04229. https://doi.org/10.1029/2010ja016245

Teng, S., Li, W., Tao, X., Ma, Q., Wu, Y., Capannolo, L., & Gan, L. (2019). Generation and characteristics of unusual high frequency EMIC waves. *Geophysical Research Letters*, *46*, 14230–14238. https://doi.org/10.1029/2019GL085220

Thorne, R. M. (2010). Radiation belt dynamics: The importance of wave-particle interactions. *Geophysical Research Letters*, *37*(22), L22107. https://doi.org/10.1029/2010GL0449902010gl044990

Thorne, R. M., Ni, B., Tao, X., Horne, R. B., & Meredith, N. P. (2010). Scattering by chorus waves as the dominant cause of diffuse auroral precipitation. *Nature*, *467*, 943–946. https://doi.org/10.1038/nature09467

Ukhorskiy, A. Y., Mauk, B. H., Fox, N. J., Sibeck, D. G., & Grebowsky, J. M. (2011). Radiation belt storm probes: Resolving fundamental physics with practical consequences. *Journal of Atmospheric and Solar-Terrestrial Physics*, *73*, 1417–1424. https://doi.org/10.1016/j.jastp.2010.12.005

Ukhorskiy, A. Y., Shprits, Y. Y., Anderson, B. J., Takahashi, K., & Thorne, R. M. (2010). Rapid scattering of radiation belt electrons by storm-time EMIC waves. *Geophysical Research Letters*, *37*, L09101. https://doi.org/10.1029/2010GL042906

Usanova, M. E., Drozdov, A., Orlova, K., Mann, I. R., Shprits, Y., Robertson, M. T., & Wygant, J. (2014). Effect of EMIC waves on relativistic and ultrarelativistic electron populations: Ground-based and Van Allen Probes observations. *Geophysical Research Letters*, *41*, 1375–1381. https://doi.org/10.1002/2013GL059024

Vainchtein, D., Zhang, X. J., Artemyev, A. V., Mourenas, D., Angelopoulos, V., & Thorne, R. M. (2018). Evolution of electron distribution driven by nonlinear resonances with intense field-aligned chorus waves. *Journal of Geophysical Research: Space Physics*, *123*(10), 8149–8169. https://doi.org/10.1029/2018JA025654

Wang, D., & Shprits, Y. Y. (2019). On how high-latitude chorus waves tip the balance between acceleration and loss of relativistic electrons. *Geophysical Research Letters*, *46*(14), 7945–7954. https://doi.org/10.1029/2019GL082681

Wang, D., Shprits, Y. Y., Zhelavskaya, I. S., Agapitov, O. V., Drozdov, A. Y., & Aseev, N. A. (2019). Analytical chorus wave model derived from Van Allen Probe observations. *Journal of Geophysical Research: Space Physics*, *124*(2), 1063–1084. https://doi.org/10.1029/2018JA026183

Wang, G., Su, Z., Zheng, H., Wang, Y., Zhang, M., & Wang, S. (2017). Nonlinear fundamental and harmonic cyclotron resonant scattering of radiation belt ultrarelativistic electrons by oblique monochromatic emic waves. *Journal of Geophysical Research: Space Physics*, *122*(2), 1928–1945. https://doi.org/10.1002/2016ja023451

Xia, Z., Chen, L., Dai, L., Claudepierre, S. G., Chan, A. A., Soto-Chavez, A. R., & Reeves, G. D. (2016). Modulation of chorus intensity by ULF waves deep in the inner magnetosphere. *Geophysical Research Letters*, *43*, 9444–9452. https://doi.org/10.1002/2016GL070280

Xia, Z., Chen, L., & Li, W. (2020). Statistical study of chorus modulations by background magnetic field and plasma density. *Geophysical Research Letters*, *47*(22), e89344. https://doi.org/10.1029/2020GL089344

Yahnin, A. G., Titova, E. E., Demekhov, A. G., Yahnina, T. A., Popova, T. A., Lyubchich, A., et al. (2020). Simultaneous observations of EMIC waves, ELF/VLF waves, and energetic particle precipitation during multiple compressions of the magnetosphere. *Geomagnetism and Aeronomy*, *59*(6), 668–680. https://doi.org/10.1134/s0016793219060148

Yahnin, A. G., Yahnina, T. A., Raita, T., & Manninen, J. (2017). Ground pulsation magnetometer observations conjugated with relativistic electron precipitation. *Journal of Geophysical Research: Space Physics*, *122*(9), 9169–9182. https://doi.org/10.1002/2017JA024249

Yahnin, A. G., Yahnina, T. A., Semenova, N. V., Gvozdevsky, B. B., & Pashin, A. B. (2016). Relativistic electron precipitation as seen by NOAA POES. *Journal of Geophysical Research: Space Physics*, *121*(9), 8286–8299. https://doi.org/10.1002/2016JA022765

Yoon, P. H., Pandey, V. S., & Lee, D.-H. (2013). Relativistic electron acceleration by oblique whistler waves. *Physics of Plasmas*, *20*(11), 112902. https://doi.org/10.1063/1.4831965

Zhang, X. J., Angelopoulos, V., Artemyev, A. V., Hartinger, M. D., & Bortnik, J. (2020). Modulation of whistler waves by ultra-low-frequency perturbations: The importance of magnetopause location. *Journal of Geophysical Research: Space Physics*, *125*(10), e28334. https://doi.org/10.1029/2020JA028334

Zhang, X.-J., Chen, L., Artemyev, A. V., Angelopoulos, V., & Liu, X. (2019). Periodic excitation of chorus and ECH waves modulated by ultra-low frequency compressions. *Journal of Geophysical Research: Space Physics*, *124*(11), 8535–8550. https://doi.org/10.1029/2019JA027201

Zhang, X. J., Li, W., Ma, Q., Thorne, R. M., Angelopoulos, V., Bortnik, J., & Fennell, J. F. (2016). Direct evidence for EMIC wave scattering of relativistic electrons in space. *Journal of Geophysical Research: Space Physics*, *121*(7), 6620–6631. https://doi.org/10.1002/2016JA022521

Zhang, X.-J., Li, W., Thorne, R. M., Angelopoulos, V., Bortnik, J., Kletzing, C. A., & Hospodarsky, G. B. (2016). Statistical distribution of EMIC wave spectra: Observations from Van Allen Probes. *Geophysical Research Letters*, *43*, 12. https://doi.org/10.1002/2016GL071158

Zhang, X. J., Mourenas, D., Artemyev, A. V., Angelopoulos, V., Bortnik, J., Thorne, R. M., & Hospodarsky, G. B. (2019). Nonlinear electron interaction with intense chorus waves: Statistics of occurrence rates. *Geophysical Research Letters*, *46*(13), 7182–7190. https://doi.org/10.1029/2019GL083833

Zhang, X.-J., Mourenas, D., Artemyev, A. V., Angelopoulos, V., & Thorne, R. M. (2017). Contemporaneous EMIC and whistler mode waves: Observations and consequences for MeV electron loss. *Geophysical Research Letters*, *44*, 8113–8121. https://doi.org/10.1002/2017GL073886

Zhang, X. J., Mourenas, D., Shen, X. C., Qin, M., Artemyev, A. V., Ma, Q., & Angelopoulos, V. (2021). Dependence of relativistic electron precipitation in the ionosphere on EMIC wave minimum resonant energy at the conjugate equator. *Journal of Geophysical Research: Space Physics*, *126*(5), e29193. https://doi.org/10.1029/2021JA029193

Zhang, X. J., Thorne, R., Artemyev, A., Mourenas, D., Angelopoulos, V., Bortnik, J., & Hospodarsky, G. B. (2018). Properties of intense field-aligned lower-band chorus waves: Implications for nonlinear wave-particle interactions. *Journal of Geophysical Research: Space Physics*, *123*(7), 5379–5393. https://doi.org/10.1029/2018JA025390